UNIVERSITY OF CALIFORNIA SAN DIEGO

Differential contributions of distinct pallidal pathways to behavioral deficits in a mouse model of Parkinson's disease

A dissertation submitted in partial satisfaction of the
requirements for the degree Doctor of Philosophy

in

Biology

by

Varoth Lilascharoen

Committee in charge:

Professor Byungkook Lim, Chair
Professor Edward M. Callaway
Professor Jeffry S. Isaacson
Professor Takaki Komiyama
Professor Nicholas C. Spitzer

2019

The Dissertation of Varoth Lilascharoen is approved, and it is acceptable in quality and form for publication on microfilm and electronically:

Chair

University of California San Diego

2019

DEDICATION

For Mom, Dad, Onn, and Grandma

EPIGRAPH

I don’t love studying. I hate studying. I like learning. Learning is beautiful.

Natalie Portman

TABLE OF CONTENTS

LIST OF FIGURES

ACKNOWLEDGMENTS

To some, graduate school is just a stepping stone to a better place in life. To me, graduate school itself is already quite a wondrous adventure. Since I started walking down this path, I have met so many wonderful souls who have helped me, through good times and bad, get to where I am today. I would like to use these following pages to express my sincere gratitude towards this marvelous group of individuals.

First of all, I am overwhelmingly grateful to have Dr. Byungkook Lim as my thesis advisor. You took such a great risk of accepting someone with so little experience like me into your lab. With your mentorship style that is as far as it could possibly be from being micromanaging, you inspired me to learn at my own pace to become independent and self-sufficient. With your support, I was able to explore this vast universe of science that greatly encouraged me to discover my passion. I would also like to acknowledge my doctoral committee members – Drs. Nick Spitzer, Takaki Komiyama, Jeff Isaacson, and Ed Callaway. Your scientific expertise and supports have been invaluable during my time at UCSD. I would like to give my special thanks to Dr. Chih-Ying Su whom I have learned a great deal from during my time as a rotation student in her lab. I would also like to acknowledge my undergraduate mentor Dr. Noppadon Kitana who introduced me to the magnificent world of neuroscience and inspired me to become both a rigorous scientist and a caring mentor. I was sponsored by Anandamahidol Foundation throughout my time in graduate school. I am forever grateful for their generous supports.

I am grateful to my fellow members of the BK Lim Lab, especially Eric, Amanda, Xiao-Yun, Stefan, Nam, Patrick, and Daniel. My project wouldn't have come this far without all your help. Apart from being a great scientist and thinker, Eric also brought out so much weirdness from the people around him. The lab has transformed dramatically (in a good way) since he became a

part of our team. He has played an extremely essential role in grooming me to become the scientist I am today. Amanda has been such a wonderful friend, colleague, and mentee since her first day in the lab. Words cannot describe how proud I am to watch her grow and become successful in her career path. To Xiao-Yun – you are the most caring person in our lab hands down. My life became so much easier since you joined the lab and took over the role of the virus maker. To Stefan and Nam – it has been a delightful experience to help mentor talented individuals like you two. To 'Patch'-trick for always sharing friendship fish with me and for being an awesome patching student. Finally, to Daniel. We had quite an adventure together as the founding members of the lab. Being able to share the ups and downs of grad school life with a fellow lab mate was such a blessing.

Here is to my friends from the UCSD Biological Sciences Ph.D. program: Angela, Nandu, Ipshita, Sachin, Mai, Yeara, Hyeseon, Bu, Mizu, Meiyan. Thank you for all the supports and beautiful friendship. I used to believe that making friends is much more difficult when you grow older. You guys proved me wrong. I am glad that we were able to share our grad school journey together. I would also like to thank Win for many hiking trips we went together and for the fun and stimulating spontaneous scientific discussions.

Last but not least, a big thank-you to my awesome family for encouraging me to become the best version of myself. I love you all so much. Thank you, Mom and Dad, for giving me so much freedom growing up and for being so incredibly supportive through all these years. To Grandma – thank you for always making sure that I have enough food to eat. To my little sister and best friend, Onn – we laugh so much whenever we are together. It's been fun having you around in the US for two years even though you were on the other side of the country. Thank you for helping me make pretty diagrams, choose the best color combinations for my PowerPoint

slides, and cell count! You are as important as all other co-authors of this work and deserve so much credit.

Chapter 1-3, in full, is currently being prepared for submission for publication of the material. Lilascharoen, Varoth; Wang, Eric; Do, Nam; Pate, Stefan; Tran, Amanda; Wang, Xiao-Yun; Park, Young-Gyun; Lim, Byungkook. The dissertation author was the primary investigator and author of this material.

VITA

2011	Bachelor of Science in Biology, Chulalongkorn University, Thailand
2011-2012	Teacher/Facilitator, Darunsikkhalai School for Innovative Learning, Thailand
2014-2017	Instructional Assistant, University of California San Diego
2019	Doctor of Philosophy in Biology, University of California San Diego

PUBLICATIONS

Barrientos, C., Knowland, D., Wu, M.M.J., Lilascharoen, V., Huang, K.W., Malenka, R.C., and Lim, B.K. (2018). Cocaine-Induced Structural Plasticity in Input Regions to Distinct Cell Types in Nucleus Accumbens. Biol Psychiatry *84*, 893-904.

Keller, J.A., Chen, J., Simpson, S., Wang, E.H., Lilascharoen, V., George, O., Lim, B.K., and Stowers, L. (2018). Voluntary urination control by brainstem neurons that relax the urethral sphincter. Nat Neurosci *21*, 1229-1238.

Knowland, D., Lilascharoen, V., Pacia, C.P., Shin, S., Wang, E.H., and Lim, B.K. (2017). Distinct Ventral Pallidal Neural Populations Mediate Separate Symptoms of Depression. Cell *170*, 284-297.e218.

Liu, J., Conde, K., Zhang, P., Lilascharoen, V., Xu, Z., Lim, B.K., Seeley, R.J., Zhu, J.J., Scott, M.M., and Pang, Z.P. (2017). Enhanced AMPA Receptor Trafficking Mediates the Anorexigenic Effect of Endogenous Glucagon-like Peptide-1 in the Paraventricular Hypothalamus. Neuron *96*, 897-909.e895.

Park, Y.G., Sohn, C.H., Chen, R., McCue, M., Yun, D.H., Drummond, G.T., Ku, T., Evans, N.B., Oak, H.C., Trieu, Choi, H., Jin, X., Lilascharoen, V., Wang, J., Truttmann, M.C., Qi, H.W., Ploegh, H.L., Golub, T., Chen, S., Frosch, M.P., Kulik, H., Lim, B.K., and Chung, K. (2018). Protection of tissue physicochemical properties using polyfunctional crosslinkers. Nat Biotechnol.

Shin, S., Pribiag, H., Lilascharoen, V., Knowland, D., Wang, X.Y., and Lim, B.K. (2018). Drd3 Signaling in the Lateral Septum Mediates Early Life Stress-Induced Social Dysfunction. Neuron *97*, 195-208.e196.

Yoo, J.H., Zell, V., Wu, J., Punta, C., Ramajayam, N., Shen, X., Faget, L., Lilascharoen, V., Lim, B.K., and Hnasko, T.S. (2017). Activation of Pedunculopontine Glutamate Neurons Is Reinforcing. J Neurosci *37*, 38-46.

Zutshi, I., Fu, M.L., Lilascharoen, V., Leutgeb, J.K., Lim, B.K., and Leutgeb, S. (2018). Recurrent circuits within medial entorhinal cortex superficial layers support grid cell firing. Nat Commun *9*, 3701.

ABSTRACT OF THE DISSERTATION

Differential contributions of distinct pallidal pathways to behavioral deficits in a mouse model of Parkinson's disease

by

Varoth Lilascharoen

Doctor of Philosophy in Biology

University of California San Diego, 2019

Professor Byungkook Lim, Chair

The external segment of the globus pallidus (GPe), a subcortical nucleus centrally located in the indirect pathway of the basal ganglia, plays a pivotal role in processing and broadcasting information received from the striatum and the subthalamic nucleus through its widespread projections across major basal ganglia nuclei. One of the largest neuronal populations of the GPe expresses the Ca^{2+}-binding protein parvalbumin (PV) and projects to multiple nuclei of the basal ganglia and the thalamus and has been shown to be involved in movement disability in Parkinson's disease (PD). However, most studies to date considered GPe PV neurons as a homogeneous

population. We found that the GPe PV neurons can be further subdivided into two non-overlapping populations based on their projections to either the substantia nigra pars reticulata (SNr) or the parafascicular thalamus (PF) and their intrinsic electrophysiological properties. We further investigated the circuit-specific roles of these subpopulations in locomotion and reversal learning as well as their contributions to the impairments of motor and behavioral flexibility in a PD mouse model. Our findings establish the behavioral significance of two distinct GPe PV neuronal populations embedded in discrete neural pathways and their differential contributions to specific subdomains of Parkinsonian-like behaviors.

INTRODUCTION

The external segment of the globus pallidus (GPe), a subcortical nucleus centrally located in the indirect pathway of the basal ganglia, plays a pivotal role in processing and broadcasting information received from the striatum and the subthalamic nucleus through its widespread projections across major basal ganglia nuclei (Kita and Kitai, 1994; Kita, 2007; Albin, Young and Penney, 1989; Bolam *et al.*, 2000; Smith *et al.*, 1998; DeLong, 1990; Mastro *et al.*, 2014). As such, GPe dysfunction may contribute to the network imbalance and behavioral deficits observed in several basal ganglia disorders, including Parkinson's disease (PD), Huntington's diseases, and obsessive-compulsive disorder through different circuits (Calabresi *et al.*, 2014; Grabli *et al.*, 2004; Correia *et al.*, 2010; Kreitzer and Berke, 2011). In PD patients and animal models of PD, the loss of nigrostriatal dopamine signaling results in movement difficulties that are accompanied by a change in GPe neural activity from uncorrelated firing to highly synchronized oscillatory bursts that is considered as one of the hallmarks of PD (Brown *et al.*, 2001; Hammond, Bergman and Brown, 2007; Mallet *et al.*, 2008b; Mallet *et al.*, 2008a; Hegeman *et al.*, 2016). Consistent with this idea, high-frequency electrical stimulation (known as deep brain stimulation; DBS) of the GPe is capable of modulating neural activity throughout the basal ganglia and has been shown to alleviate motor disability in both human patients and primate PD model (Johnson *et al.*, 2012; Vitek *et al.*, 2004; Vitek *et al.*, 2012). While it is well accepted that the maladaptive changes of the GPe could be involved in PD, it is unknown how each GPe circuit contributes to behavioral functions and whether each circuit is affected in PD.

The GPe contains mostly GABAergic neurons that can be classified as being either arkypallidal or prototypic based on their efferent connectivity and *in vivo* neural activity (Abdi *et al.*, 2015; Mallet *et al.*, 2012). The arkypallidal neurons provide an extensive striatal innervation,

while the prototypic neurons predominantly innervate downstream basal ganglia nuclei. The majority of the prototypic neurons express the Ca^{2+}-binding protein parvalbumin (PV) and project to multiple nuclei of the basal ganglia and the thalamus, including the subthalamic nucleus (STN), substantia nigra pars reticulata (SNr), internal segment of the globus pallidus (GPi; entopeduncular nucleus in rodents), and the parafascicular nucleus of the thalamus (Kita, 2007; Dodson *et al.*, 2015; Hernández *et al.*, 2015; Mastro *et al.*, 2014). Among the projections of the GPe PV neurons, the SNr, as an output nucleus of the basal ganglia, plays an important role in mediating diverse motor functions (Hikosaka, Nakamura and Nakahara, 2006), whereas the PF is primarily thought to support behavioral flexibility during reversal learning (Brown, Baker and Ragozzino, 2010; Ding *et al.*, 2010; Bradfield *et al.*, 2013; Kato *et al.*, 2011; Kato *et al.*, 2018; Birrell and Brown, 2000; Smith *et al.*, 2011) as well as motor control (Smith *et al.*, 2014; Parker, Lalive and Kreitzer, 2016). While this suggests that the GPe PV neurons could mediate different behavioral functions depending on their target structures, whether or not the GPe projections to the SNr and PF represent separate subpopulations is unknown.

Here, we investigate circuit-specific roles of the GPe PV neurons in locomotion and reversal learning as well as their contributions to the impairments of these behavioral functions in a PD mouse model. We first found that the GPe PV neurons can be subdivided into two non-overlapping populations based on their projections to either the SNr or PF and their intrinsic electrophysiological properties. We demonstrated that modulation of the SNr-projecting GPe PV neurons bidirectionally influenced locomotor activity but had no major effect on reversal learning. On the other hand, activation of the PF-projecting GPe PV neurons impaired reversal learning but did not affect locomotion. Finally, we showed that selective activation of the SNr-projecting GPe PV neurons rescued the motor deficit, whereas the inhibition of the PF-projecting GPe PV neurons

only rescued the impaired behavioral flexibility in dopamine-depleted mice. Taken together, these findings establish the behavioral significance of two distinct GPe PV neuronal populations embedded in discrete neural pathways and their differential contributions to specific behavioral deficits in parkinsonian state.

CHAPTER 1

RESULTS

GPe PV neurons projecting to the SNr or PF represent distinct subpopulations

The anatomical tracing from previous reports indicated that GPe PV neurons send their axonal projections to multiple brain structures in the basal ganglia and the thalamus (Beier *et al.*, 2017; Mastro *et al.*, 2014). However, the target structures were identified by fluorescence quantification of labeled axons which could not distinguish between axon-of-passage and actual synaptic sites. To address this issue, we injected an adeno-associated virus (AAV) expressing a red fluorescent protein, mRuby2, and synaptophysin fused with eGFP in Cre-dependent manner into the GPe of PV^{Cre} mice. With this approach, the synapses are specifically labeled with eGFP, allowing us to discriminate between putative presynaptic terminals and the mRuby2-labeled axons (Knowland *et al.*, 2017). Brains were processed using SHIELD-MAP method to preserve fluorescence and to allow visualization of GPe PV axons and synapses in intact brain tissue (Figure 1A; Park *et al.*, 2018). Consistent with previous findings, we observed robust labeling of synaptic puncta in the STN, SNr, EP, PF and sparser labeling in the dorsal striatum (Figure 1B; Mastro *et al.*, 2014; Saunders, Huang and Sabatini, 2016). However, we did not observe extensive labeling of both the axons and presynaptic terminals of GPe PV neurons in other regions of the thalamus as previously reported (Beier *et al.*, 2017).

Given the widespread output projections, we next asked whether individual GPe PV neurons collateralize to multiple targets, or different subpopulations project to distinct targets (Figure 1C). Among those projections, the SNr, as an output nucleus of the basal ganglia, plays an important role in mediating diverse motor functions (Hikosaka, Nakamura and Nakahara, 2006), whereas the PF is primarily thought to support flexibility during reversal learning (Brown, Baker

and Ragozzino, 2010; Ding *et al.*, 2010; Bradfield *et al.*, 2013; Kato *et al.*, 2011; Kato *et al.*, 2018). These different functions led us to hypothesize that the axon terminals we observed in the SNr and PF arise from different subsets of the GPe PV neurons. To test this, we developed and adapted a novel viral vector capable of neuron-specific retrograde infection by pseudotyping an equine infectious anemia lentivirus (EIAV) with a fusion protein (FuG-B2) carrying extracellular and transmembrane domains of the rabies glycoprotein connected to the cytoplasmic domain of vesicular stomatitis virus glycoprotein (RG-EIAV) to label cells defined by their projection target (Figure 1D; Knowland *et al.*, 2017; Cetin and Callaway, 2014; Kato and Kobayashi, 2014). In PV^{Cre} mice, we injected the SNr or PF with RG-EIAV expressing Flp recombinase in a Cre-dependent manner (RG-EIAV-DIO-Flp) and injected the GPe with an AAV inducing Flp-dependent expression of eGFP (AAV-fDIO-eGFP; Figure 1D). The results indicated that the SNr-projecting GPe PV neurons ($PV^{GPe\text{-}SNr}$) collateralize to other nuclei in the basal ganglia, including the STN, EP, and dorsal striatum while the PF-projecting GPe PV neurons ($PV^{GPe\text{-}PF}$) innervate the PF exclusively without making any collaterals (Figure 1E). We also found that $PV^{GPe\text{-}SNr}$ and $PV^{GPe\text{-}PF}$ neurons localize specifically to the dorsolateral and ventromedial regions of the GPe, respectively (Figure S1).

$PV^{GPe\text{-}SNr}$ and $PV^{GPe\text{-}PF}$ neurons are electrophysiologically distinct

Several studies have shown that neurons in the pallidal areas display heterogeneous autonomous firing patterns and intrinsic membrane properties based on their projection targets (Knowland *et al.*, 2017; Saunders *et al.*, 2015; Abdi *et al.*, 2015; Wallace *et al.*, 2017). To test whether $PV^{GPe\text{-}SNr}$ and $PV^{GPe\text{-}PF}$ neurons differ in their electrophysiological properties, we performed visualized *ex vivo* whole-cell recordings in acute brain slices. We selectively labeled only $PV^{GPe\text{-}SNr}$ and $PV^{GPe\text{-}PF}$ neurons by using an intersectional strategy where we injected an RG-

EIAV expressing Cre in a Flp-dependent manner (RG-EIAV-fDIO-Cre) into either SNr or PF of *PV^{Flp} x Ai14* mice, resulting in projection-specific tdTomato expression in GPe PV neurons (Figure 2A; Knowland et al, 2017). The majority of both populations was spontaneously active at rest with the PV$^{GPe\text{-}SNr}$ neurons firing regularly at a higher average rate and the PV$^{GPe\text{-}PF}$ neurons at a comparatively lower rate with more spike timing variability as assessed by the coefficient of variation of the inter-spike interval (CV_{ISI}; Figure 2B-D). To determine the firing capacity, we injected depolarizing current until neurons went into depolarization block. PV$^{GPe\text{-}SNr}$ neurons exhibit a fast-spiking behavior as indicated by their higher maximum firing rate and driven activity across the entire range of current pulses compared with the PV$^{GPe\text{-}PF}$ neurons (Figure 2E-F). In line with this, our analysis of action potential waveforms revealed that PV$^{GPe\text{-}PF}$ neurons exhibit a significantly higher action potential threshold, a wider half-width, and a longer afterhyperpolarization potential (AHP) latency (Figure I-L). In summary, in addition to their different anatomical organization, PV$^{GPe\text{-}SNr}$ and PV$^{GPe\text{-}PF}$ neurons also differ in their electrophysiological properties.

PV$^{GPe\text{-}SNr}$ and PV$^{GPe\text{-}PF}$ neurons have different afferent connectivity patterns

Our results thus far strongly distinguish PV$^{GPe\text{-}PF}$ neurons PV$^{GPe\text{-}SNr}$ neurons both anatomically and electrophysiologically. Therefore, we hypothesized that they may have distinct brain-wide input patterns as well. We probed the input-output organization of GPe PV neurons by cell-type and projection-specific trans-synaptic tracing. We injected RG-EIAV-DIO-Flp into either the SNr or PF, then AAVs expressing TVA receptor and an optimized rabies glycoprotein in Flp-dependent manner (AAV-fDIO-TVA-mRuby, AAV-fDIO-oPBG, respectively) into GPe of *PV^{Cre}* mice (Figure 3A, B). We subsequently injected EnvA-pseudotyped, glycoprotein-deleted

rabies virus (RVΔG-eGFP-(EnvA)) into the GPe to map monosynaptic inputs to these two populations (Figure 3A, B).

Whole-brain quantification of eGFP-labeled neurons revealed differences in input patterns of $PV^{GPe\text{-}SNr}$ and $PV^{GPe\text{-}PF}$ neuronal populations. While both populations receive most of their inputs from the dorsal striatum, $PV^{GPe\text{-}SNr}$ neurons receive proportionally more inputs from the STN, whereas $PV^{GPe\text{-}PF}$ neurons receive more inputs from the cortex and the SNr. This further suggests that $PV^{GPe\text{-}SNr}$ and $PV^{GPe\text{-}PF}$ neurons participate in differential circuits of the basal ganglia. We also noticed that proportionally more neurons from the dorsomedial striatum (DMS) project to $PV^{GPe\text{-}PF}$ neurons, while more neurons from the dorsolateral striatum (DLS) project to $PV^{GPe\text{-}SNr}$ neurons. Since the DMS and DLS were shown to be involved in different behavioral functions, $PV^{GPe\text{-}SNr}$ and $PV^{GPe\text{-}PF}$ neurons may receive and transmit differential information that mediates different behaviors. In contrast to the classical model of the basal ganglia, a recent study indicated that axon collaterals of striatal direct-pathway medium spiny neurons (dMSNs) are also present in the GPe (Cazorla *et al.*, 2014). As such, we determined whether the striatal neurons projecting to $PV^{GPe\text{-}SNr}$ and $PV^{GPe\text{-}PF}$ neurons are dMSNs or iMSNs by performing *in situ* hybridization to label *Drd1a* and *Drd2* mRNA. We found that $PV^{GPe\text{-}SNr}$ neurons receive proportionally more inputs from iMSNs, while $PV^{GPe\text{-}PF}$ neurons receive more inputs from dMSNs, further suggesting that $PV^{GPe\text{-}SNr}$ and $PV^{GPe\text{-}PF}$ neurons are parts of distinct GPe circuits (Figure 3D-E).

$PV^{GPe\text{-}SNr}$ and $PV^{GPe\text{-}PF}$ neurons mediate different behavioral functions

The activity of rodent SNr and PF neurons have been shown to be involved in a range of behavioral functions including motor control and behavioral flexibility, respectively (Hikosaka, Nakamura and Nakahara, 2006; Brown, Baker and Ragozzino, 2010). Given the distinct upstream connectivity patterns and electrophysiological properties, $PV^{GPe\text{-}SNr}$ and $PV^{GPe\text{-}PF}$ neurons could

convey differential information toward their respective targets. Therefore, we hypothesized that $PV^{GPe\text{-}SNr}$ and $PV^{GPe\text{-}PF}$ neurons may have different roles in locomotion and reversal learning. We first determined whether the increased activity of $PV^{GPe\text{-}SNr}$ and $PV^{GPe\text{-}PF}$ neurons directly promotes movement. We employed two approaches: optogenetic activation and chemogenetic inhibition of $PV^{GPe\text{-}SNr}$ and $PV^{GPe\text{-}PF}$ neurons. We first expressed oChIEF, a fast variant of channelrhodopsin with higher conductivity (Lin *et al.*, 2009), in GPe PV neurons and bilaterally stimulated their axon terminals in the SNr or PF while measuring the locomotor activity in an open field (Figure 4A). The optical stimulation paradigm (500 ms-pulses, repeated every 1.5 s) was determined by testing the efficacy of a range of stimulation frequencies that can reliably inhibit spiking activity of SNr neurons *ex vivo* and was used throughout this study. During a 10-minute activation of $PV^{GPe\text{-}SNr}$ axon terminals, average locomotor activity as assessed by speed was markedly increased and was elevated beyond the stimulation period whereas $PV^{GPe\text{-}PF}$ activation did not show any changes (Figure 4B-C).

We next tested the effect of silencing $PV^{GPe\text{-}SNr}$ and $PV^{GPe\text{-}PF}$ neurons on locomotion by expressing an inhibitory chemogenetic receptor (hM4Di) in each population. Because the behavioral tests we performed in this study required prolonged inhibition of neural activity in projection-defined populations, we utilized chemogenetic inhibition instead of optogenetic inhibition due to the issue on the efficacy of optogenetic inhibition at presynaptic terminals raised by a recent study (Mahn *et al.*, 2016). We achieved this by bilaterally injecting AAV-fDIO-hM4Di-mCherry into the GPe and RG-EIAV-DIO-Flp into the SNr or PF (Figure 4D). Following CNO treatment, mice in which hM4Di was expressed in $PV^{GPe\text{-}SNr}$ neurons showed a significant reduction in locomotor activity while silencing $PV^{GPe\text{-}PF}$ neurons did not show any effects on

locomotion (Figure 4E-F). Thus, our results suggest that the activity of $PV^{GPe\text{-}SNr}$ neurons but not $PV^{GPe\text{-}PF}$ neurons can bidirectionally influence locomotion.

We next investigated whether modulation of each subpopulation can affect the behavioral performance in the cue-guided learning task. The animals were food-deprived and subjected to a naturalistic foraging reversal discrimination task which consists of two consecutive phases. First, in the association phase, mice were trained to associate a certain cue with a rewarding outcome, and a different cue without reward until they can discriminate reliably. In the subsequent reversal learning phase, the cue-outcome associations were reversed, and thus, the mice needed to switch their actions to obtain the reward (Birrell and Brown, 2000; Bissonette *et al.*, 2008; Bissonette *et al.*, 2015). A criterion is met when a block of ten consecutive trials contains at least eight correct trials (80% accuracy). Mice were first trained to discriminate reward and non-reward cues as mentioned above, and either projection-specific optogenetic activation or chemogenetic inhibition were employed during the reversal learning phase. While the optical stimulation of oChIEF-expressing GPe PV axons in the SNr showed no effect, the stimulation of GPe PV axons in the PF significantly increased the number of trials needed to successfully acquire reversal learning, indicating that the mice had more trouble switching and that the behavioral flexibility was profoundly impaired (Figure 5B-C). However, silencing both $PV^{GPe\text{-}SNr}$ and $PV^{GPe\text{-}PF}$ neurons during reversal learning phase did not alter the reversal performance (Figure 5E-F).

Distinct GPe PV circuitries are involved in different physiological and behavioral deficits observed in a neurotoxin-induced PD mouse model

The differential effects of projection-specific manipulation of $PV^{GPe\text{-}SNr}$ and $PV^{GPe\text{-}PF}$ neurons on locomotion and reversal learning suggest that these circuitries are involved in different phenotypes observed in a PD mouse model (Grospe, Baker and Ragozzino, 2018; Parker, Lalive

and Kreitzer, 2016). We, therefore, reasoned that $PV^{GPe\text{-}SNr}$ and $PV^{GPe\text{-}PF}$ neurons may exhibit distinct neural adaptations to dopamine depletion. To address this, we performed cell-attached and whole-cell recordings in $PV^{GPe\text{-}SNr}$ and $PV^{GPe\text{-}PF}$ neurons in acute brain slices obtained from mice that were injected with 6-hydroxydopamine (6-OHDA) in the medial forebrain bundle (MFB). We observed a significant reduction in autonomous firing rate in $PV^{GPe\text{-}SNr}$ neurons (Figure 6B), but not in $PV^{GPe\text{-}PF}$ neurons (Figure 6C), which was restored to normal when synaptic transmission was blocked by AMPA receptor and GABA-A receptor antagonists (NBQX and picrotoxin, respectively), suggesting that a net change in afferent synaptic activity underlies this adaptation in $PV^{GPe\text{-}SNr}$ neurons. Furthermore, we examined whether synaptic transmission from the terminals of $PV^{GPe\text{-}SNr}$ and $PV^{GPe\text{-}PF}$ neurons onto their targets were altered as a result of dopamine depletion. We replaced extracellular Ca^{2+} with Sr^{2+} and optogenetically stimulated GPe PV axon terminals while recording from SNr and PF neurons to allow measurement of quantal-like events from the stimulated synapses (Oliet, Malenka and Nicoll, 1996). Interestingly, we observed a significant decrease in the frequency of optogenetically-evoked quantal-like inhibitory postsynaptic currents (qIPSC) in SNr neurons, while that in the PF neurons is markedly increased (Figure 6H). Taken together, we reasoned that the different neural adaptation in $PV^{GPe\text{-}SNr}$ and $PV^{GPe\text{-}PF}$ neurons may differentially contribute to behavioral changes in dopamine-depleted mice.

Based on the physiological changes we observed in $PV^{GPe\text{-}SNr}$ and $PV^{GPe\text{-}PF}$ neurons in dopamine-depleted mice, we tested whether enhancing or suppressing the activity of $PV^{GPe\text{-}SNr}$ and $PV^{GPe\text{-}PF}$ according to their alterations due to dopamine depletion can rescue behavioral deficits in this animal model. We first focused on bradykinesia which is a hallmark of parkinsonian motor deficits. We hypothesized that compensating the net reduction of $PV^{GPe\text{-}SNr}$ synaptic output by optogenetic activation can restore locomotor activity in dopamine-depleted mice. Indeed, we

observed a robust increase in locomotion in bilaterally depleted mice (Figure S2) during a 10-minute stimulation period where we selectively activated axonal fibers of $PV^{GPe\text{-}SNr}$ neurons in the SNr. The locomotor activity was restored to approximately 50-60% of the baseline activity assessed before 6-OHDA infusion and persisted beyond the stimulation period for at least 20 minutes (Figure 7B).

Besides the motor deficits, many PD patients and animal models also display cognitive flexibility impairment even in the early stage of the disease (Grospe, Baker and Ragozzino, 2018; Cools *et al.*, 2001; Peterson *et al.*, 2009). Given that increased activity of $PV^{GPe\text{-}PF}$ neurons impairs reversal learning (Figure 4C) and that the strength of their synapses in the PF is enhanced in response to dopamine depletion, it is possible that the physiological adaptation of $PV^{GPe\text{-}PF}$ neurons contributes to the cognitive flexibility impairment in the early stage of dopamine loss in PD. To this end, we assessed the behavioral flexibility with the cue-guided reversal-learning task three days after bilateral 6-OHDA infusion to mimic the early stage of dopamine depletion at which the mice did not show a clear sign of locomotor deficits (Figure S2), allowing them to properly learn the task. Consistent with previous reports, the dopamine-depleted mice can initially acquire simple discrimination but reversal learning was greatly impaired (Grospe, Baker and Ragozzino, 2018). We then selectively inhibited $PV^{GPe\text{-}PF}$ neurons with chemogenetics during the reversal learning period where mice in all groups received CNO treatment (5 mg/kg). Remarkably, CNO treatment significantly improved the reversal performance comparable to that observed in control (Figure 7D).

Collectively, these experiments reveal that each of the two subpopulations undergoes specific adaptation in response to dopamine depletion which contributes to a separate behavioral deficit observed in different parkinsonian states.

Figure 1. Distinct subpopulations of GPe PV neurons project to the SNr and PF.

(A) 3D rendering of a cleared mouse hemisphere showing projection patterns of GPe PV neurons.

(B) Representative confocal images of the injection site in GPe (top left) and target structures showing axonal fibers in magenta and synaptic puncta in green. Scale bar, 30 μm.

(C) Two possible projection patterns: GPe PV neurons collateralizes to all targets (top), or distinct subpopulations send projections to specific targets (bottom).

(D) Schematic of viral strategy. EIAV is pseudotyped with a fusion protein containing rabies virus glycoprotein and VSVG transmembrane protein (RG-EIAV). RG-EIAV-DIO-Flp is injected into the target area and AAV-fDIO-eGFP into GPe of PV^{Cre} mice.

(E) Images of injection site and target areas showing cell-type- and projection-specific labeling. GPe PV neurons selectively project to either the SNr or PF, respectively, but not to both. Scale bar, 100 μm.

EIAV, equine infectious anemia virus; RV-G, rabies virus glycoprotein; TRN, thalamic reticular nucleus; EP, entopeduncular nucleus; STN, subthalamic nucleus.

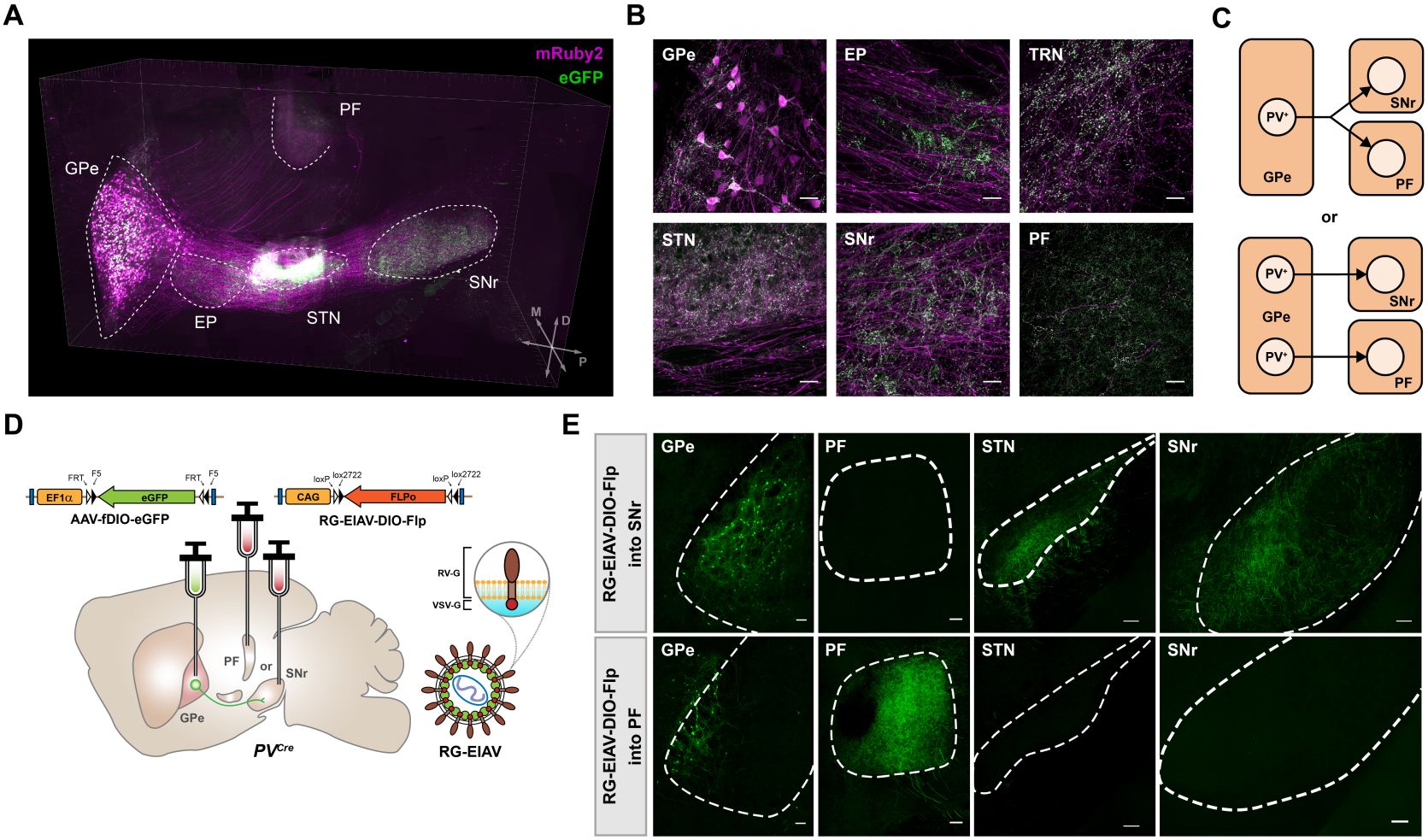
A
mRuby2
eGFP
PF
GPe
SNr
EP
STN
M
D
P
B
GPe
EP
TRN
STN
SNr
PF
C
PV+
GPe
SNr
PF
or
PV+
GPe
PV+
SNr
PF
D
FRT
F5
EF1α
eGFP
AAV-fDIO-eGFP
loxP
lox2722
CAG
FLPo
RG-EIAV-DIO-Flp
RV-G
VSV-G
PF
or
SNr
GPe
PVCre
RG-EIAV
E
RG-EIAV-DIO-Flp into SNr
RG-EIAV-DIO-Flp into PF
GPe
PF
STN
SNr

Figure 2. $PV^{GPe\text{-}SNr}$ and $PV^{GPe\text{-}PF}$ neurons exhibit distinct electrophysiological properties.

(A) Strategy using *PV^{Flp} x Ai14* mouse for labeling GPe PV neurons in projection-specific manner. RG-EIAV-fDIO-Cre is injected into either SNr or PF.

(B) Representative cell-attached recordings from $PV^{GPe\text{-}SNr}$ and $PV^{GPe\text{-}PF}$ neurons.

(C) Autonomous firing rate of $PV^{GPe\text{-}SNr}$ and $PV^{GPe\text{-}PF}$ neurons. Mann-Whitney *U*-test, U = 7; ***$p < 0.001$ ($n = 22$ cells for $PV^{GPe\text{-}SNr}$ and $n = 17$ cells for $PV^{GPe\text{-}PF}$ neurons).

(D) Firing regularity of $PV^{GPe\text{-}SNr}$ and $PV^{GPe\text{-}PF}$ neurons. Mann-Whitney *U*-test, U = 7; **$p = 0.0019$ ($n = 22$ cells for $PV^{GPe\text{-}SNr}$ and $n = 17$ cells for $PV^{GPe\text{-}PF}$ neurons).

(E) Representative traces of spikes in response to 100pA, 200pA, and 300pA current injections in $PV^{GPe\text{-}SNr}$ and $PV^{GPe\text{-}PF}$ neurons.

(F) Action potential firing frequency in response to a range of current injections for $PV^{GPe\text{-}SNr}$ and $PV^{GPe\text{-}PF}$ neurons. Gray shading shows a significant difference ($p < 0.05$). Multiple *t*-test, corrected for multiple comparisons using Holm-Sidak method ($n = 21$ cells for $PV^{GPe\text{-}SNr}$ and $n = 24$ cells for $PV^{GPe\text{-}PF}$ neurons).

(G) Maximum firing rate of $PV^{GPe\text{-}SNr}$ and $PV^{GPe\text{-}PF}$ neurons. Mann-Whitney *U*-test, U = 23; ***$p < 0.001$ ($n = 21$ cells for $PV^{GPe\text{-}SNr}$ and $n = 24$ cells for $PV^{GPe\text{-}PF}$ neurons).

(H) Membrane capacitance of $PV^{GPe\text{-}SNr}$ and $PV^{GPe\text{-}PF}$ neurons. Mann-Whitney *U*-test, U = 23; ***$p < 0.001$ ($n = 21$ cells for $PV^{GPe\text{-}SNr}$ and $n = 24$ cells for $PV^{GPe\text{-}PF}$ neurons).

(I) Representative traces of action potential waveforms for $PV^{GPe\text{-}SNr}$ and $PV^{GPe\text{-}PF}$ neurons.

(J) Action potential threshold of $PV^{GPe\text{-}SNr}$ and $PV^{GPe\text{-}PF}$ neurons. Mann-Whitney *U*-test, U = 57; ***$p < 0.0001$ ($n = 21$ cells for $PV^{GPe\text{-}SNr}$ and $n = 24$ cells for $PV^{GPe\text{-}PF}$ neurons).

(K) Action potential half-width of $PV^{GPe\text{-}SNr}$ and $PV^{GPe\text{-}PF}$ neurons. Mann-Whitney *U*-test, U = 10; ***$p < 0.001$ ($n = 21$ cells for $PV^{GPe\text{-}SNr}$ and $n = 24$ cells for $PV^{GPe\text{-}PF}$ neurons).

(L) Afterhyperpolarization latency of $PV^{GPe\text{-}SNr}$ and $PV^{GPe\text{-}PF}$ neurons. Mann-Whitney *U*-test, U = 32; ***$p < 0.001$ ($n = 21$ cells for $PV^{GPe\text{-}SNr}$ and $n = 24$ cells for $PV^{GPe\text{-}PF}$ neurons). All data presented as mean ± SEM.

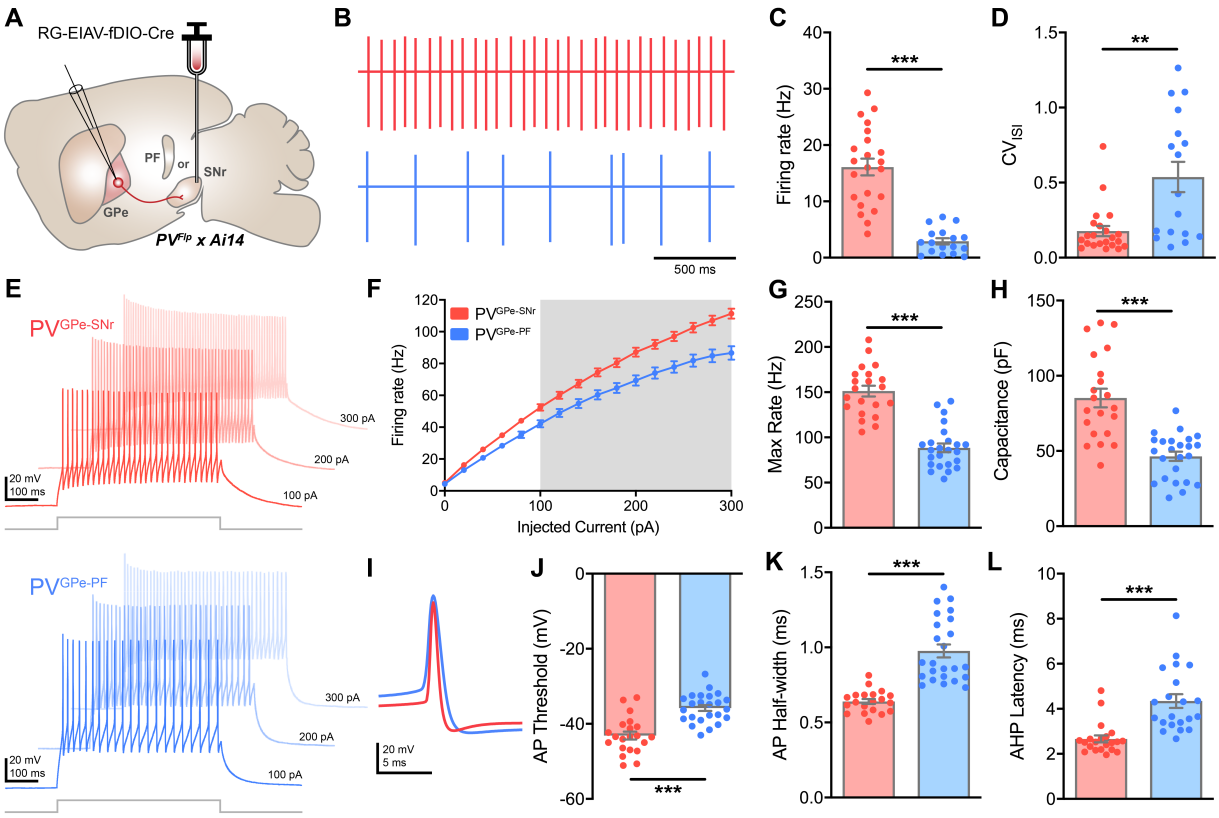
A
RG-EIAV-fDIO-Cre
PF
or
SNr
GPe
PVFlp x Ai14
B
500 ms
C
Firing rate (Hz)
***
D
CVISI
**
E
PVGPe-SNr
300 pA
200 pA
100 pA
20 mV
100 ms
PVGPe-PF
F
PVGPe-SNr
PVGPe-PF
Firing rate (Hz)
Injected Current (pA)
G
Max Rate (Hz)
***
H
Capacitance (pF)
***
I
20 mV
5 ms
J
AP Threshold (mV)
***
K
AP Half-width (ms)
***
L
AHP Latency (ms)
***

Figure 3. Whole-brain mapping of inputs to $PV^{GPe\text{-}SNr}$ and $PV^{GPe\text{-}PF}$ neurons reveals partially overlapping afferent matrices and distinct striatal inputs.

(A) Viral strategy to map pseudotyped rabies-mediated monosynaptic inputs to $PV^{GPe\text{-}SNr}$ neurons (top). Representative images of select brain areas (bottom). Scale bars, 500 μm; inset 50 μm.

(B) Viral strategy to map pseudotyped rabies-mediated monosynaptic inputs to $PV^{GPe\text{-}PF}$ neurons (top). Representative images of select brain areas (bottom). Scale bars, 500 μm; inset 50 μm.

(C) Whole-brain quantification of inputs to $PV^{GPe\text{-}SNr}$ and $PV^{GPe\text{-}PF}$ neurons. Data presented as percentage of total cells in a given brain area relative to the total number of brain-wide inputs. Unpaired *t*-tests used for individual brain regions, $*p < 0.05$, $**p < 0.01$ ($n = 3$ mice for each subpopulation).

(D) Images of striatal neurons sending input to $PV^{GPe\text{-}SNr}$ and $PV^{GPe\text{-}PF}$ neurons with cell-type-specific markers. Arrows represent colocalization between input neurons labeled by the rabies virus and mRNA for the specified probe. Scale bar, 10 μm.

(E) Quantification of *Drd1a*$^+$ or *Drd2*$^+$ striatal inputs to $PV^{GPe\text{-}SNr}$ and $PV^{GPe\text{-}PF}$ neurons. Paired *t*-test, $t(2) = 9.333$; $*p = 0.0113$ ($n = 3$ mice for each subpopulation)

M2, secondary motor cortex; dStr, dorsal striatum; CeA, central amygdala; DRN, dorsal raphe nucleus. All data presented as mean ± SEM.

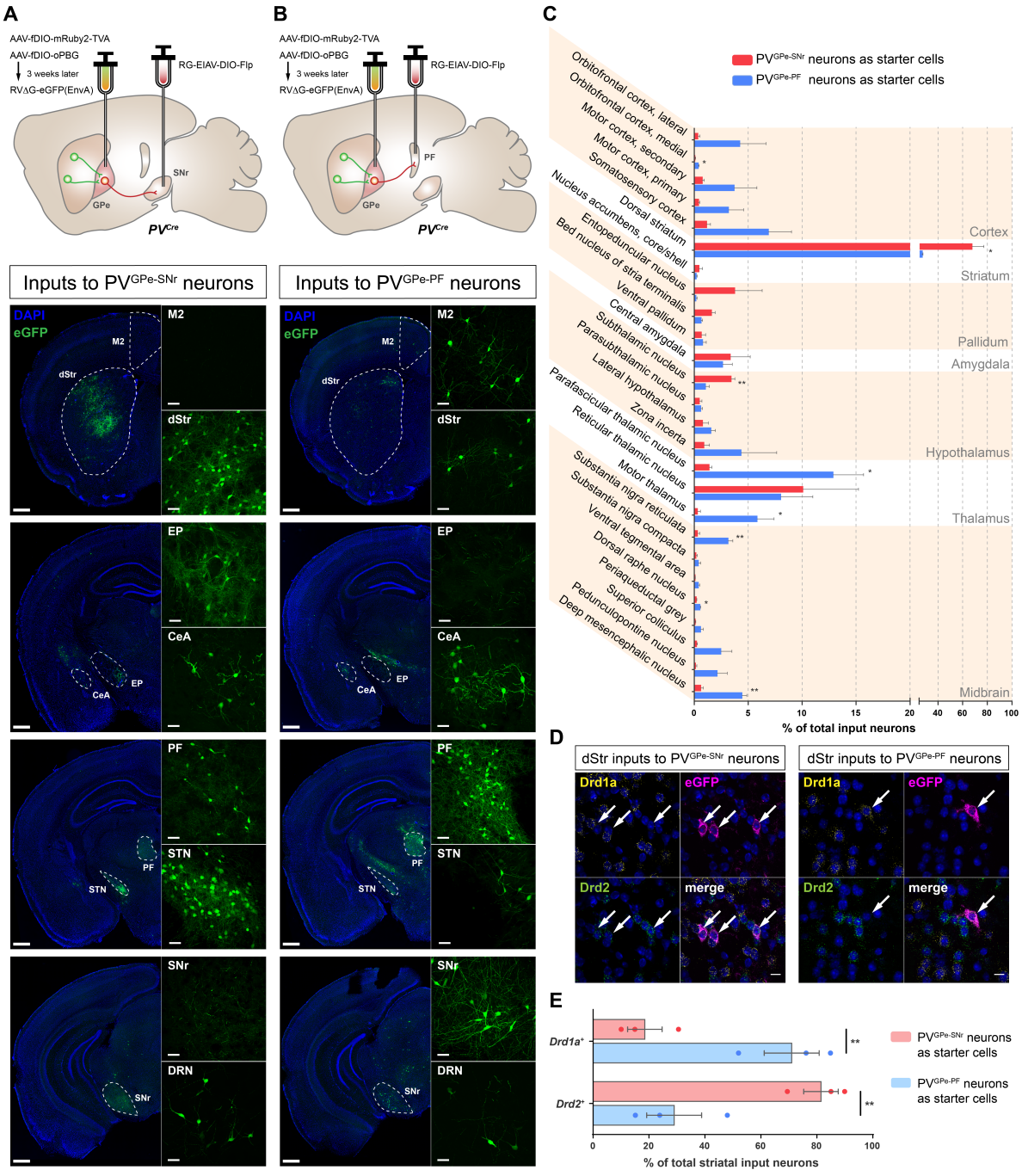
A
AAV-fDIO-mRuby2-TVA
AAV-fDIO-oPBG
3 weeks later
RVΔG-eGFP(EnvA)
RG-EIAV-DIO-Flp
SNr
GPe
PVCre
B
AAV-fDIO-mRuby2-TVA
AAV-fDIO-oPBG
3 weeks later
RVΔG-eGFP(EnvA)
RG-EIAV-DIO-Flp
PF
GPe
PVCre
Inputs to PVGPe-SNr neurons
Inputs to PVGPe-PF neurons
DAPI
eGFP
M2
dStr
EP
CeA
PF
STN
SNr
DRN
C
PVGPe-SNr neurons as starter cells
PVGPe-PF neurons as starter cells
Orbitofrontal cortex, lateral
Orbitofrontal cortex, medial
Motor cortex, secondary
Motor cortex, primary
Somatosensory cortex
Dorsal striatum
Nucleus accumbens, core/shell
Entopeduncular nucleus
Bed nucleus of stria terminalis
Ventral pallidum
Central amygdala
Subthalamic nucleus
Parasubthalamic nucleus
Lateral hypothalamus
Zona incerta
Parafascicular thalamic nucleus
Reticular thalamic nucleus
Motor thalamus
Substantia nigra reticulata
Substantia nigra compacta
Ventral tegmental area
Dorsal raphe nucleus
Periaqueductal grey
Superior colliculus
Pedunculopontine nucleus
Deep mesencephalic nucleus
Cortex
Striatum
Pallidum
Amygdala
Hypothalamus
Thalamus
Midbrain
% of total input neurons
D
dStr inputs to PVGPe-SNr neurons
dStr inputs to PVGPe-PF neurons
Drd1a
eGFP
Drd2
merge
E
Drd1a+
Drd2+
PVGPe-SNr neurons as starter cells
PVGPe-PF neurons as starter cells
% of total striatal input neurons

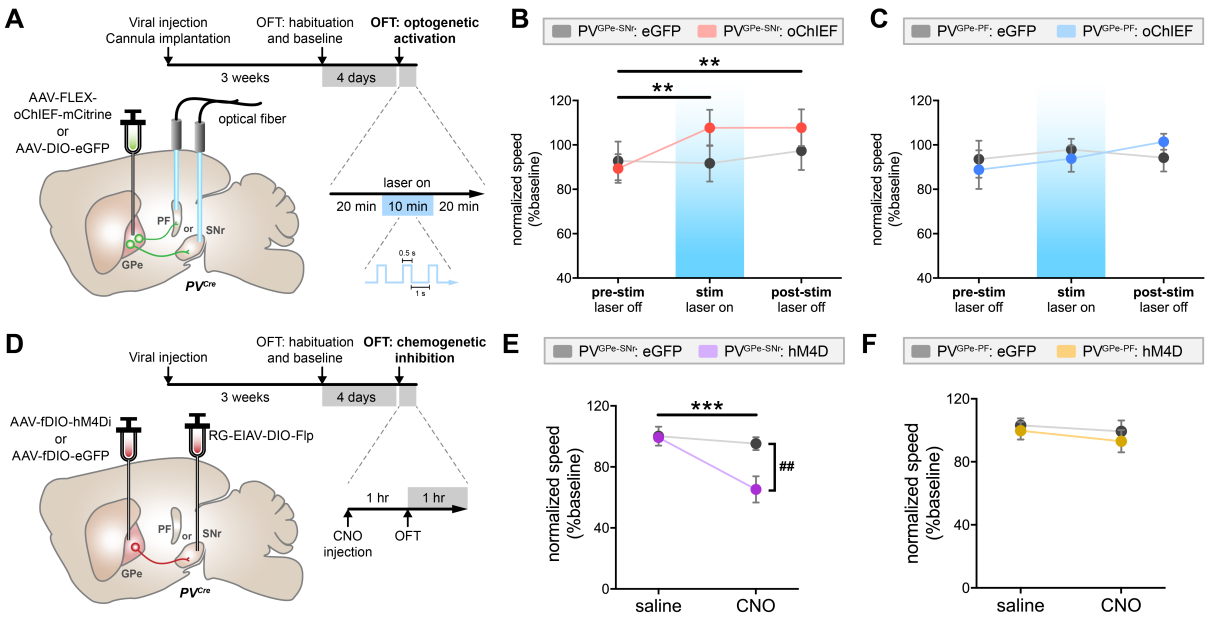

Figure 4. Activation and silencing of PV$^{GPe\text{-}SNr}$ neurons bidirectionally influence locomotion

(A) Schematic of viral injections and optic fiber implantations, experimental timeline, and stimulation protocol for optogenetic activation.

(B) Activation of GPe PV terminal in the SNr increased locomotion during stimulation and post-stimulation periods. Two-way repeated-measures ANOVA, main effect$_{stimxgroup}$: $F(2,36) = 3.863$, $p = 0.0302$; main effect$_{stim}$: $F(2,36) = 5.513$, $p = 0.0082$; main effect$_{group}$: $F(1, 18) = 0.5161$, $p = 0.4817$; Bonferroni's *post hoc* test, $^{**}p < 0.01$; $n = 10$ mice for both GFP and oChIEF).

(C) Activation of GPe PV terminal in the PF showed no major effect on locomotion. Two-way repeated-measures ANOVA, main effect$_{stimxgroup}$: $F(2,26) = 0.6664$, $p = 0.5221$; main effect$_{stim}$: $F(2,26) = 0.6870$, $p = 0.5120$; main effect$_{group}$: $F(1, 13) = 0.0065$, $p = 0.9368$; $n = 7$ mice for GFP and $n = 8$ mice for oChIEF).

(D) Schematic of viral injections and experimental timeline for cell-type- and projection-specific expression of inhibitory DREADD (hM4Di) in PV$^{GPe\text{-}SNr}$ and PV$^{GPe\text{-}PF}$ neurons.

(E) Inhibition of PV$^{GPe\text{-}SNr}$ neurons suppresses locomotion. Two-way repeated-measures ANOVA, main effect$_{treatmetxgroup}$: $F(1,18) = 9.644$, $p = 0.0061$; main effect$_{treatment}$: $F(1,18) = 17.30$, $p = 0.0006$; main effect$_{group}$: $F(1, 18) = 4.968$, $p = 0.0388$; Bonferroni's *post hoc* test, $^{***}p < 0.0001$; $^{\#\#}p = 0.002$; $n = 10$ mice for both GFP and hM4D).

(F) Inhibition of PV$^{GPe\text{-}PF}$ neurons showed no major effect on locomotion. Two-way repeated-measures ANOVA, main effect$_{treatmetxgroup}$: $F(1,10) = 0.069$, $p = 0.7980$; main effect$_{treatment}$: $F(1,10) = 0.9681$, $p = 0.3484$; main effect$_{group}$: $F(1, 10) = 0.5119$, $p = 0.4911$; $n = 6$ mice for both GFP and hM4D). All data presented as mean ± SEM.

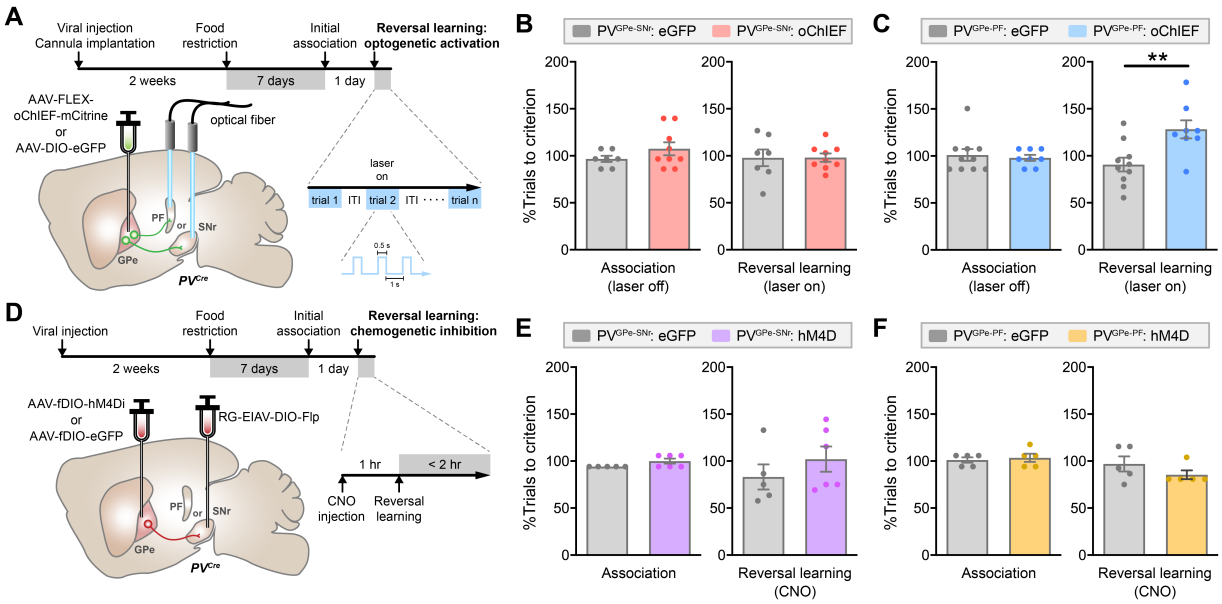

Figure 5. Activation of PV$^{GPe\text{-}PF}$ neurons impairs behavioral flexibility in reversal learning

(A) Schematic of viral injections and optic fiber implantations, experimental timeline, and stimulation protocol for optogenetic activation during reversal learning.

(B) Activation of GPe PV terminal in the SNr during reversal showed no major effect on behavioral flexibility. Unpaired *t*-test, $t(16) = 0.0273$, $p = 0.9786$; $n = 7$ mice for GFP and $n = 9$ oChIEF).

(C) Activation of GPe PV terminal in the PF during reversal learning impaired behavioral flexibility. Unpaired *t*-test, $t(16) = 3.142$, $^{**}p = 0.0063$; $n = 10$ mice for GFP and $n = 8$ oChIEF).

(D) Schematic of viral injections and experimental timeline for cell-type- and projection-specific expression of inhibitory DREADD (hM4Di) in PV$^{GPe\text{-}SNr}$ and PV$^{GPe\text{-}PF}$ neurons.

(E) Inhibition of PV$^{GPe\text{-}SNr}$ neurons during reversal learning showed no major effect on behavioral flexibility. Unpaired *t*-test, $t(9) = 0.9840$, $p = 0.3508$; $n = 5$ mice for GFP and $n = 6$ hM4D).

(F) Inhibition of PV$^{GPe\text{-}PF}$ neurons during reversal learning showed no major effect on behavioral flexibility. Unpaired *t*-test, $t(8) = 1.245$, $p = 0.2483$; $n = 5$ mice for both GFP and hM4D). All data presented as mean ± SEM.

Figure 6. $PV^{GPe\text{-}SNr}$ and $PV^{GPe\text{-}PF}$ neurons exhibit distinct electrophysiological adaptations to dopamine depletion

(A) Schematic of viral and 6-OHDA injections and the experimental timeline for the recording of $PV^{GPe\text{-}SNr}$ and $PV^{GPe\text{-}PF}$ neurons in acute slices after dopamine depletion.

(B) Autonomous firing rate in $PV^{GPe\text{-}SNr}$ neurons from naïve control and dopamine-depleted mice with and without synaptic transmission blockers, NBQX and picrotoxin (PTX) in extracellular solution (Kruskal-Wallis *H* test, $p = 0.0130$; Dunn's post hoc test, $*p < 0.05$; control $n = 20$ cells, OHDA $n = 27$ cells, control (with blockers) $n = 34$ cells, OHDA (with blockers) $n = 59$ cells)

(C) Autonomous firing rate in $PV^{GPe\text{-}PF}$neurons from naïve control and dopamine-depleted mice with and without synaptic transmission blockers, NBQX and picrotoxin (PTX) in extracellular solution (Kruskal-Wallis *H* test, $p = 0.8203$; control $n = 11$ cells, OHDA $n = 19$ cells, control (with blockers) $n = 20$ cells, OHDA (with blockers) $n = 15$ cells)

(D) Schematic of viral and 6-OHDA injections for the recording of optically-evoked quantal-like inhibitory postsynaptic currents (qIPSC) in SNr and PF neurons in acute slices after dopamine depletion.

(E) Example trace (upper) showing evoked qIPSC in SNr neuron elicited by stimulation of GPe-PV terminals. Red trace represents a fitted curve generated by Python script. qIPSC amplitudes were measured from subtracted trace (lower) from 0-400 ms after stimulation.

(F) Representative subtracted traces of optically-evoked qIPSC in SNr and PF neurons from naïve control and dopamine depleted mice.

(G) Amplitudes of optically-evoked qIPSC in SNr and PF neurons were not altered by dopamine depletion. Mann-Whitney *U*-test, $U = 41$, $p = 0.3824$ for SNr; $U = 14$, $p = 0.6389$ for PF (SNr control $n = 12$ cells, SNr OHDA $n = 9$ cells; PF control $n = 5$ cells, PF OHDA $n = 7$ cells).

(H) Frequency of optically-evoked qIPSC was decreased and increased in SNr and PF neurons, respectively. Mann-Whitney *U*-test, $U = 26$, $p = 0.0491$ for SNr; $U = 2$, $p = 0.0101$ for PF (SNr control $n = 12$ cells, SNr OHDA $n = 9$ cells; PF control $n = 5$ cells, PF OHDA $n = 7$ cells). All data presented as mean ± SEM.

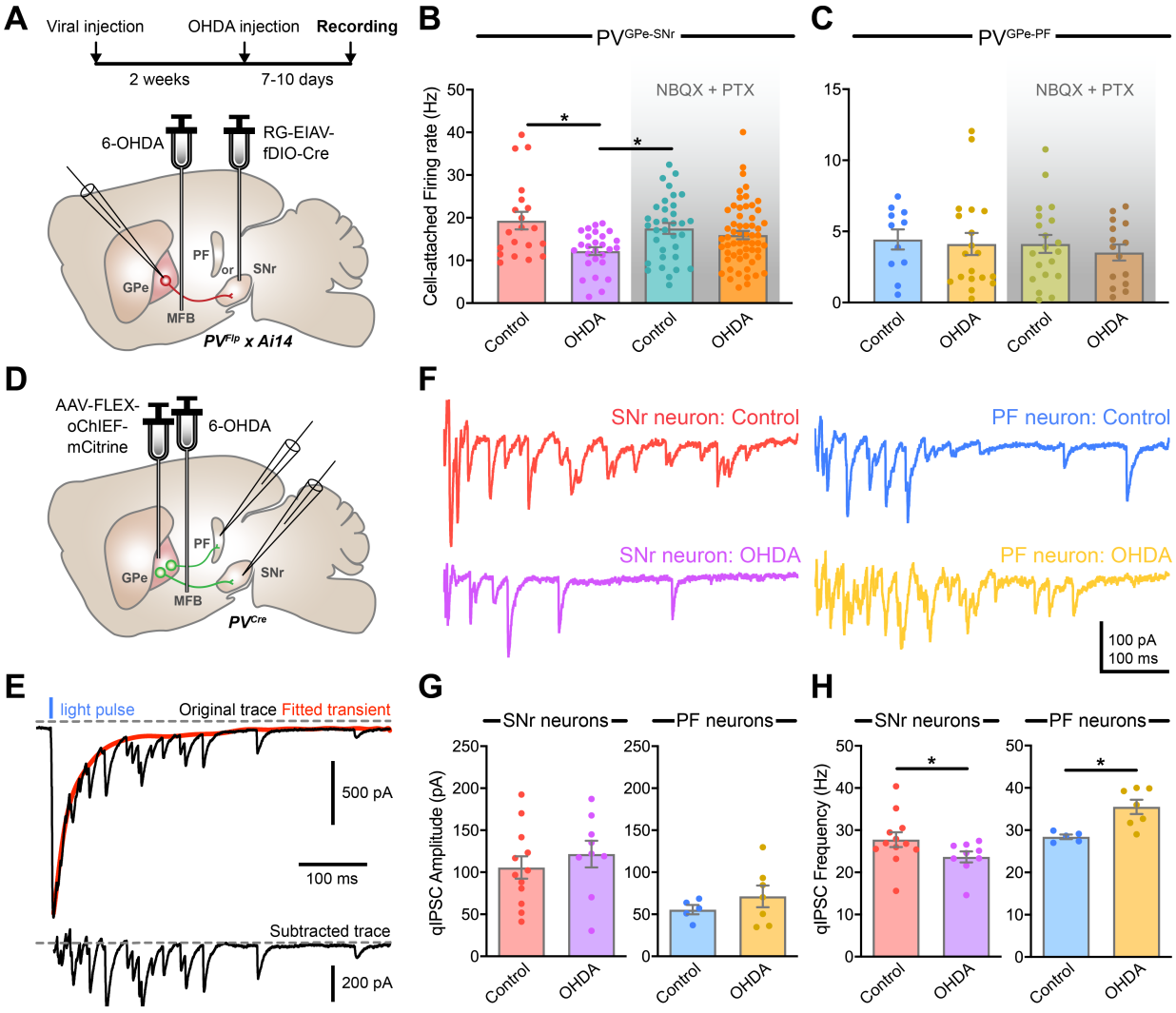
A
Viral injection
OHDA injection
Recording
2 weeks
7-10 days
6-OHDA
RG-EIAV-
fDIO-Cre
PF
or
SNr
GPe
MFB
PVFlp x Ai14
B
PVGPe-SNr
NBQX + PTX
Cell-attached Firing rate (Hz)
Control
OHDA
Control
OHDA
C
PVGPe-PF
NBQX + PTX
Control
OHDA
Control
OHDA
D
AAV-FLEX-
oChIEF-
mCitrine
6-OHDA
PF
GPe
SNr
MFB
PVCre
F
SNr neuron: Control
PF neuron: Control
SNr neuron: OHDA
PF neuron: OHDA
100 pA
100 ms
E
light pulse
Original trace
Fitted transient
500 pA
100 ms
Subtracted trace
200 pA
G
SNr neurons
PF neurons
qIPSC Amplitude (pA)
Control
OHDA
Control
OHDA
H
SNr neurons
PF neurons
qIPSC Frequency (Hz)
Control
OHDA
Control
OHDA

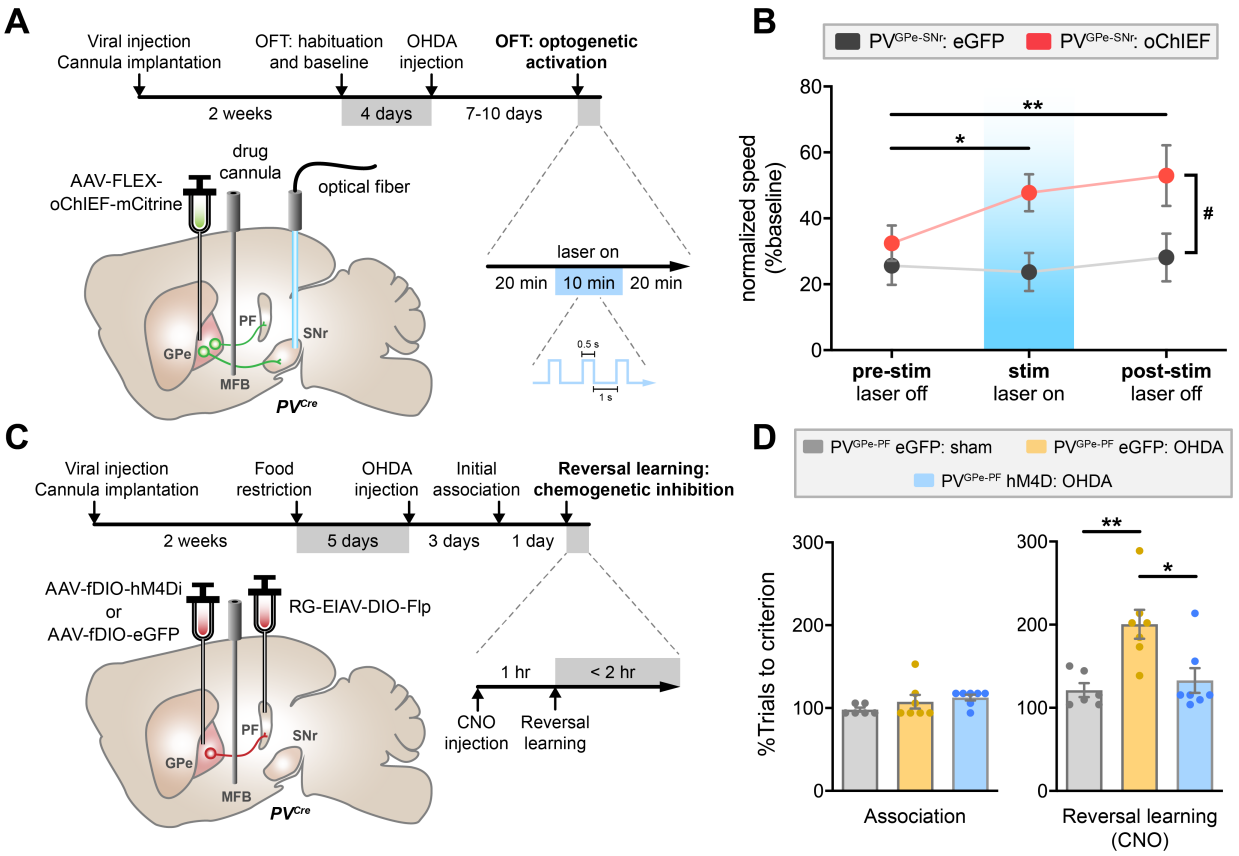

Figure 7. PV$^{GPe\text{-}SNr}$ and PV$^{GPe\text{-}PF}$ neurons mediate different behavioral deficits in dopamine-depleted mice

(A) Schematic of viral injections, optic fiber, and drug cannula implantations, experimental timeline, and stimulation protocol for optogenetic activation during locomotion after dopamine depletion.

(B) Activation of GPe PV terminal in the SNr restored locomotor activity during stimulation and post-stimulation periods in dopamine-depleted mice. Two-way repeated-measures ANOVA, main effect$_{stimxgroup}$: $F(2,38) = 2.691$, $p = 0.0807$; main effect$_{stim}$: $F(2,38) = 3.460$, $p = 0.0417$; main effect$_{group}$: $F(1, 19) = 5.436$, $p = 0.0309$; Bonferroni's *post hoc* test, $^{\#}p < 0.05$, $*p < 0.05$, $**p < 0.01$; GFP $n = 10$ mice, oChIEF $n = 11$ mice).

(D) Schematic of viral injections and drug cannula implantations, and experimental timeline for cell-type- and projection-specific expression of inhibitory DREADD (hM4Di) in PV$^{GPe\text{-}PF}$ neurons.

(E) Inhibition of PV$^{GPe\text{-}PF}$ neurons during reversal learning improved behavioral flexibility in dopamine-depleted mice. One-way ANOVA, $F(2,17) = 8.642$, $p = 0.0026$; Bonferroni's *post hoc* test, $*p = 0.0114$, $**p = 0.0046$; GFP-vehicle $n = 6$ mice, GFP-OHDA $n = 7$ mice, hM4D-OHDA $n = 7$ mice). All data presented as mean ± SEM.

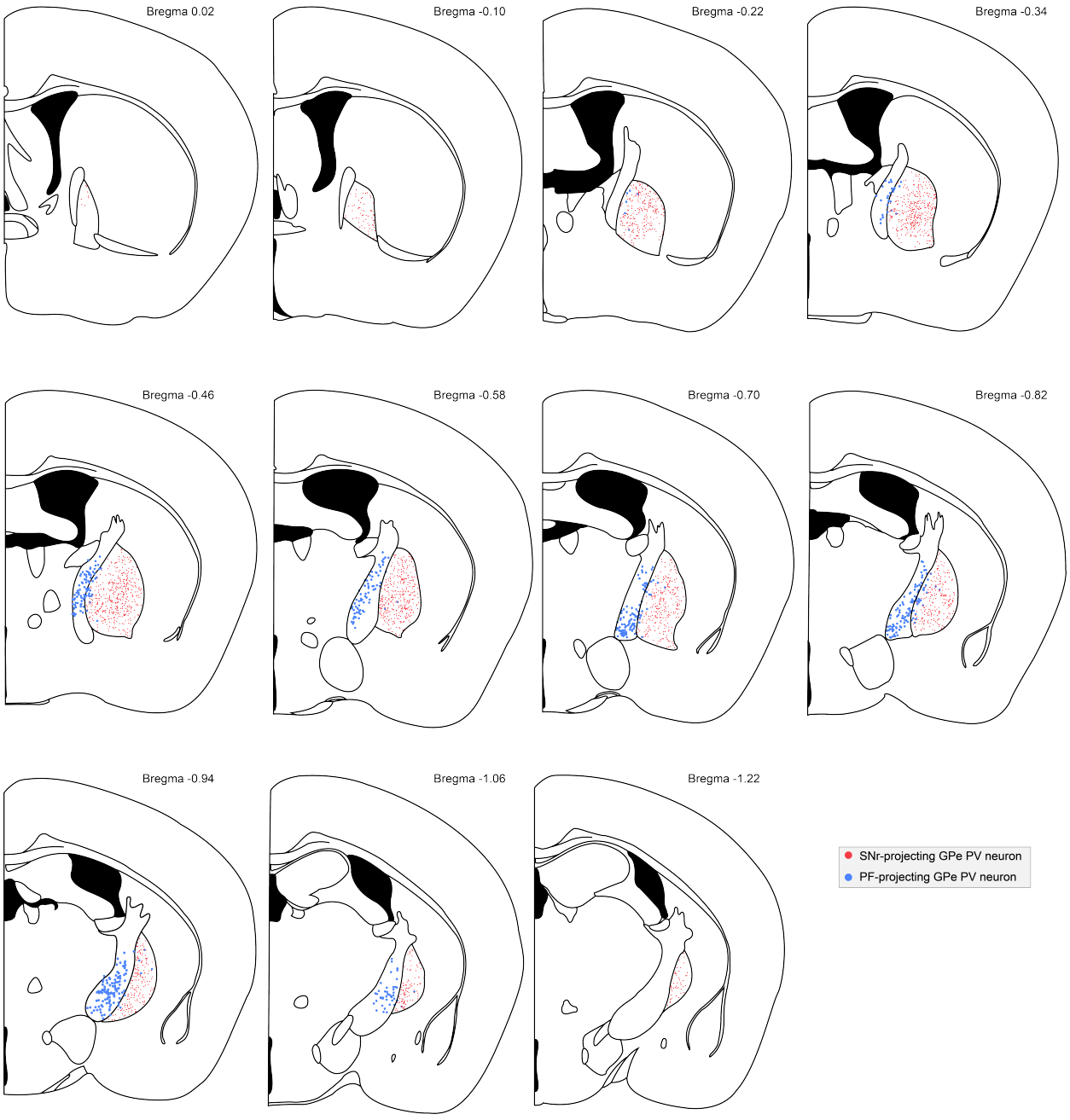

Figure S1. Anatomical localization of $PV^{GPe\text{-}SNr}$ and $PV^{GPe\text{-}PF}$ neurons, related to Figure 1.

Localization of $PV^{GPe\text{-}SNr}$ (red) and $PV^{GPe\text{-}PF}$ (blue) neurons across the A-P axis in the GPe. Only cells in the GPe are shown. Each dot represents a single neuron. All neurons presented are cumulative across 3 mice for each population.

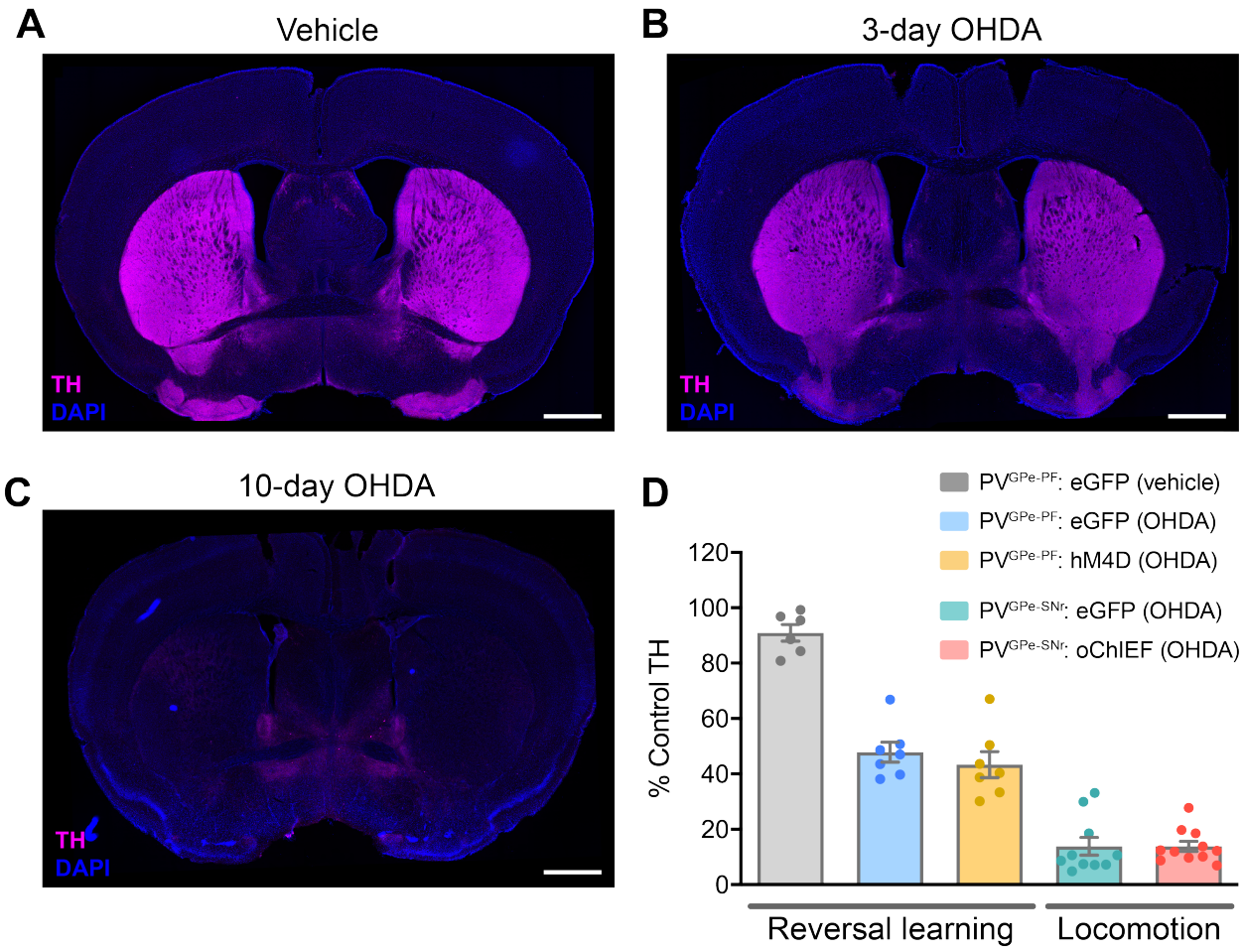

Figure S2. Quantification of TH immunoreactivity, related to Figure 7.

(A) Representative image of TH immunoreactivity in the striatum of a mouse injected with vehicle (0.02% sodium ascorbate in 0.9% saline). Scale bar, 1 mm.

(B) Representative image of TH immunoreactivity in the striatum 3 days after bilateral 6-OHDA injection. Scale bar, 1 mm.

(C) Representative image of TH immunoreactivity in the striatum 10 days after bilateral 6-OHDA injection. Scale bar, 1 mm.

(D) Quantification of TH immunoreactivity at different stages of dopamine depletion in rescue experiments for reversal learning and locomotion. Data presented as % mean ± SEM of naïve control striatal sections.

Chapter 1, in full, is currently being prepared for submission for publication of the material. Lilascharoen, Varoth; Wang, Eric; Do, Nam; Pate, Stefan; Tran, Amanda; Wang, Xiao-Yun; Park, Young-Gyun; Lim, Byungkook. The dissertation author was the primary investigator and author of this material.

CHAPTER 2

DISCUSSION

Diversity of GPe neurons and their distinct roles in motor function and behavioral flexibility

Using complementary electrophysiological, viral-mediated tracing, and behavioral approaches, we have presented evidence that distinct circuits in the GPe are involved in different basal ganglia-related behaviors and that physiological adaptation of each circuit contributes to different behavioral deficit observed in a mouse model of PD. Our viral-mediated tracing clearly showed that GPe PV neurons can be distinguished based on their projections to either SNr or PF. These two subpopulations display topographical preference within the GPe, in which the $PV^{GPe\text{-}PF}$ neurons are located more medial relative to the $PV^{GPe\text{-}SNr}$ neurons (Figure S1). Interestingly, we found that the $PV^{GPe\text{-}PF}$ neurons preferentially receive inputs from dMSNs, but not iMSNs, in the dorsal medial part of the striatum, suggesting that distinct GPe circuits can convey different striatal information to their projection targets. This finding contradicts the classical model of the basal ganglia which suggests that the GPe receives its striatal input exclusively from the indirect pathway (Albin, Young and Penney, 1989; Albin, Young and Penney, 1995). The studies of the basal ganglia behavioral functions have been focused largely on the output structures, SNr and GPi, which strongly influence the activity of the thalamocortical loop during movement (Alexander, Crutcher and DeLong, 1990; Haber and Calzavara, 2009). However, the roles of the direct output of GPe to the thalamus has not been fully characterized. In contrast to the GPe-SNr pathway involvement in locomotion, we found that the GPe-PF pathway is highly involved in behavioral flexibility during reversal learning. This suggests that although the activity of basal ganglia circuitry is associated with a wide range of behaviors, the specific roles of microcircuits within the basal ganglia can be different. Consistent with this notion, a recent study has

demonstrated that the striatum can be subdivided into more than 20 different regions based on their anatomical input and output organization (Hintiryan *et al.*, 2016), which further emphasizes the need of investigation on the role of individual microcircuit in the basal ganglia.

The engagement of distinct basal ganglia circuitry in different PD states

The progression of PD is commonly evaluated by the severity of motor symptoms, however, non-motor symptoms, such as difficulties in planning or behavioral flexibility that can also occur at different stages of PD are also common. How different brain circuitries involve in motor or non-motor symptoms of PD has not been fully elucidated. Here, we demonstrated that, in 6-OHDA-injected animals, dopamine depletion induced differential synaptic alteration at different target structures of GPe PV neurons. By artificially compensating these changes in synaptic transmission, we were able to rescue locomotor deficits and behavioral inflexibility at different stages of parkinsonian states, indicating that the neural adaptations in different circuits in response to dopamine depletion may underlie the progressive nature of PD. Our reasoning is further strengthened by our anatomical mapping which shows that the $PV^{GPe\text{-}SNr}$ and $PV^{GPe\text{-}PF}$ neurons receive different brain-wide inputs, suggesting that they may participate in distinct pathways of the basal ganglia by routing relevant information to their respective targets. Since we demonstrated that the GPe-PF pathway is important for maintaining a new action-outcome association during reversal learning, manipulating the activity of this pathway could provide a novel treatment strategy for ameliorating behavioral inflexibility in PD. We believe that our findings establish the behavioral significance of two distinct GPe PV neuronal populations embedded in discrete neural pathways and their differential contributions to specific subdomains of Parkinsonian-like behaviors that occur at different stages of the disease. These results also suggest that further elucidation on the detailed synaptic connectivity of the GPe that links together

different subdomains of the GPe downstream targets is needed to fully understand the circuit-specific role of the basal ganglia which could provide better therapeutic strategies for the treatment of PD.

Chapter 2, in full, is currently being prepared for submission for publication of the material. Lilascharoen, Varoth; Wang, Eric; Do, Nam; Pate, Stefan; Tran, Amanda; Wang, Xiao-Yun; Park, Young-Gyun; Lim, Byungkook. The dissertation author was the primary investigator and author of this material.

CHAPTER 3

MATERIALS AND METHODS

Animals

All procedures to maintain and use mice were approved by the Institutional Animal Care and Use Committee (IACUC) at the University of California, San Diego. Mice were maintained on a 12-hour light/dark cycle with regular mouse chow and water available *ad libitum* except when placed under food restriction. All behavioral experiments were performed during the dark cycle. PV^{Cre}, *Ai14* (Rosa26-CAG-LSL-tdTomato), and PV^{Flp} transgenic mice were obtained from the Jackson Laboratory (JAX strain 008069, 007914, and 22730, respectively) and were maintained on a C57BL/6J background. PV^{Flp} *x Ai14* transgenic mice were generated by crossing PV^{Flp} mice with *Ai14* mice. For all experiments, male and female heterozygous mice aged 8-20 weeks were used.

Viral vectors

AAV plasmids were constructed using standard molecular cloning methods. Synaptophysin-eGFP, oPBG, hM4D(Gi)-mCherry, and TVA DNA fragments were obtained from pAAV-phSyn1(S)-FLEX-tdTomato-T2A-SypEGFP-WPRE (a gift from Hongkui Zeng; Addgene plasmid #51509), pAAV-hSyn-DIO-hM4D(Gi)-mCherry (a gift from Bryan Roth; Addgene plasmid #44362), pAAV-EF1α-DIO-oPBG (a gift from Edward M. Callaway), and pAAV-EF1α-FLEX-GTB (a gift from Edward M. Callaway; Addgene plasmid #26197), respectively. pAAV-FLEX-oChIEF-mCitrine was a gift from Roger Tsien (Addgen plasmid #50973). A Flp-dependent, double-floxed, inverted open reading frame (fDIO) was constructed with two heterospecific pairs of FRT and FRT5 sequences based on pAAV-EF1α-fDIO-hChR2(H134R)-eYFP (a gift from Karl Deisseroth; Addgene plasmid #55639). We used EF1α promoter to drive the expression of target

constructs for all AAV vectors except for AAV-DIO-mRuby2-T2A-Synaptophysin-eGFP, AAV-fDIO-hM4D(Gi)-mCherry, and AAV-FLEX-oChIEF-mCitrine which are driven by the human synapsin promoter.

All AAV vectors used in this study were packaged as serotype DJ and generated as previously described (Lim *et al.*, 2012). In brief, AAV vectors were produced by transfection of AAV293 cells (Agilent) with three plasmids: an AAV vector plasmid carrying target constructs (DIO-mRuby2-T2A-Synaptophysin-eGFP, DIO-eGFP, fDIO-eGFP, fDIO-oPBG, fDIO-mRuby2-P2A-TVA, fDIO-hM4D(Gi)-mCherry, or FLEX-oChIEF-mCitrine), AAV helper plasmid (pHELPER; Agilent), and AAV rep-cap helper plasmid (pRC-DJ, gift from M. Kay). At 72 h post-transfection, the cells were collected and lysed by a repeated freeze-thaw procedure. Viral particles were then purified by an iodixanol step-gradient ultracentrifugation and subsequently concentrated using a 100-kDa molecular cutoff ultrafiltration device (Millipore). The genomic titer was determined by quantitative PCR. The AAV vectors were diluted in PBS to a working concentration of approximately 10^{13} viral particles/ml.

EIAV genomic vector plasmids were constructed from pEIAV-SIN6.1-CBGFPW (a gift from John Olsen; Addgene #44173) by replacing eGFP coding sequence with DNA fragments containing either DIO-FlpO or fDIO-Cre. RG-EIAV vectors were generated by a modified version of a published protocol (Cetin and Callaway, 2014). Briefly, HEK293-T cells were transfected with three plasmids: an EIAV genomic vector (pEIAV-CAG-DIO-Flp or pEIAV-CAG-fDIO-Cre), a helper packaging plasmid (pEV53B; a gift from Edward M. Callaway), and a pseudotyping plasmid encoding fusion protein FuG-B2 (a gift from Kazuto Kobayashi). At 72 h post-transfection, viral particles were harvested from the media by centrifugation using SureSpin630 swinging bucket rotor (Thermo Scientific) at 5,700 rpm and 16,200 rpm for 16 h and 2 h,

respectively. EIAV viral particles were reconstituted from the pellets with PBS and immediately stored at -80°C.

Rabies virus was generated as previously described (Osakada and Callaway, 2013) from a full-length cDNA plasmid containing all components of the virus except the coding sequence of the rabies glycoprotein which was replaced with eGFP (a gift from Karl-Klaus Conzelmann). In brief, B7GG cells were transfected with a total of five plasmids: four plasmids expressing the viral components pcDNA-SADB16N, pcDNA-SADB16P, pcDNA-SADB16L, pcDNA-SADB16G, and the rabies virus genomic vector. The virus-containing media was collected 3-4 days post-transfection and used for further amplification. Viral particles were harvested from the media by centrifugation using SureSpin630 rotor at 20,000 rpm for 2 h. Rabies viral particles were reconstituted from the pellets with PBS and immediately stored at -80°C. To generate EnvA-pseudotyped, glycoprotein-deleted rabies virus expressing eGFP (RVΔG-eGFP(EnvA)), we used a modified version of a published protocol (Osakada and Callaway, 2013). BHK-EnvA cells were grown in four 15-cm dishes to 50-60% confluency. The cells were transduced with the rabies virus expressing eGFP generated in the previous step. After 3 hours, the media was removed and the cells were rinsed with PBS, trypsinized for 5 min at 37°C, and isolated by pipetting repeatedly with a P1000 pipettor. Each dish was observed carefully under the microscope to ensure that the cells did not aggregate. The cells were then pelleted by centrifugation and plated in four new dishes. Trypsinization was repeated two more times at 9 and 21 hours after transduction to ensure complete removal of the original rabies glycoprotein. The virus-containing media was collected 4 days post-transduction and concentrated as described above. Plasmids expressing the rabies viral components, B7GG, BHK-EnvA, and HEK-TVA cells were gifts from Edward M. Callaway.

Stereotaxic viral injections and optic fiber/cannula implantation

Mice were anesthetized with a mixture of ketamine (100 mg/kg) and dexmedetomidine (1 mg/kg) and placed on a stereotaxic frame (David Kopf Instruments). The body temperature was maintained with a heating pad during surgery and recovery from anesthesia. All stereotactic coordinates were derived from Paxinos and Franklin mouse brain atlas. Viruses were infused into the brain by using pulled glass micropipettes coupled with a syringe pump (PHD ULTRA; Harvard Apparatus) at a rate of 100 nl/min. For tracing experiment to visualize output regions of GPe PV neurons, 150 nl of AAV-FLEX-mRuby2-T2A-Synaptophysin-eGFP was injected into the GPe of PV^{Cre} mice (anteroposterior -0.35 mm, mediolateral 1.95 mm from bregma, and depth -3.5 mm from brain surface). For cell-type- and projection-specific tracing, 500 nl of RG-EIAV-DIO-Flp was unilaterally injected into either SNr (anteroposterior -3.25 mm, mediolateral 1.6 mm from bregma, and depth -4.4 mm from brain surface) or PF (anteroposterior -2.15 mm, mediolateral 0.625 mm from bregma, and depth -3.1 mm from brain surface) of PV^{Cre} mice along with 350 nl of AAV-fDIO-eGFP into ipsilateral GPe. After allowing 3 weeks of expression, mice were euthanized for circuit mapping analysis.

For mapping of input-output relationship, 500 nl of RG-EIAV-DIO-Flp was unilaterally injected into either SNr or PF of PV^{Cre} mice along with 350 nl of a 1:1 mixture of AAV-fDIO-oPBG and AAV-fDIO-mRuby2-P2A-TVA into ipsilateral GPe. After allowing 3 weeks of expression, animals were again anesthetized as previously described and 350 nl of RVΔG-eGFP(EnvA) was injected into ipsilateral GPe. Mice were euthanized after 7 days for quantification of input neurons and *in situ* hybridization.

For electrophysiological recordings of GPe neurons, 500 nl of RG-EIAV-fDIO-Cre was unilaterally injected into either SNr or PF of PV^{Flp} *x Ai14* mice. For recordings of postsynaptic

neurons in SNr and PF, 350 nl of AAV-FLEX-oChIEF-mCitrine was unilaterally injected into the GPe of PV^{Cre} mice. After allowing 3 weeks of expression, acute slices were prepared for recordings.

For optogenetic behavioral experiments, PV^{Cre} mice were bilaterally injected with 350 nl of AAV-FLEX-oChIEF-mCitrine (or AAV-DIO-eGFP for controls) into the GPe. Subsequently, a bilateral 26-gauge guide cannula (cut length 4.5 mm, center-to-center distance 2 mm; Plastic One) was implanted over the medial forebrain bundle (MFB; anteroposterior -0.5 mm, mediolateral 1.0 mm from bregma) for 6-hydroxydopamine infusion and was temporally secured in place with cyanoacrylate glue. Optic fibers (200 μm, 0.22 NA; Doric Lenses) were cut to length (4.5 mm for SNr and 3.5 mm for PF) and implanted bilaterally above SNr (depth 4.0 mm from brain surface) or PF (mediolateral angle 15°, anteroposterior -2.15 mm, mediolateral -1.65 from bregma, depth -3.0 mm from brain surface) during the same surgery session. The optic fibers and the guide cannula were secured in place with a layer of adhesive cement (Radiopaque L-powder for C&B Metabond; Parkell). Once dried, absorbable sutures and a second layer of dental cement (Ortho-Jet; Lang Dental) were used to seal the head incision. For chemogenetic behavioral experiments, 500 nl of RG-EIAV-DIO-Flp was bilaterally injected into either SNr or PF of PV^{Cre} mice along with 350 nl AAV-fDIO-hM4D(Gi)-mCherry (or AAV-fDIO-eGFP for controls) into the GPe. During the same surgery session, a bilateral guide cannula was implanted over the MFB as described above. Behavioral experiments were performed 4 weeks after surgery to allow time recovery and optimal viral expression. Upon completion of behavioral experiments, viral injections, optic fiber and guide cannula placements were confirmed with histology to ensure proper targeting.

Dopamine depletion

6-hydoxydopamine (6-OHDA) solution was freshly prepared by adding 6-OHDA HCl (Sigma) to an appropriate volume of sterile saline (0.9% NaCl) with 0.02% sodium ascorbate (Sigma) to achieve the desired concentration. To prevent lesioning of non-dopamine monoaminergic neurons, desipramine (25 mg/kg) was injected intraperitoneally 30 min before 6-OHDA injection (Breese and Traylor, 1971).

6-OHDA injection for electrophysiological recordings was performed with the same method mentioned above two weeks after viral injection. Mice were anesthetized with isoflurane (2% in O_2) and 750 nl of 6-OHDA solution (2.5 μg/μl) was unilaterally injected into the MFB (anteroposterior -0.5 mm, mediolateral 1.0 mm from bregma, depth -4.8 mm from brain surface) at a rate of 150 nl/min. For behavioral experiments after dopamine depletion, 2-3 weeks after surgery (see 'behavioral assay' for experimental timelines), mice were anesthetized with isoflurane (2% in O_2) and a 33-gauge bilateral injector (cut length 5 mm; Plastic One) attached to a syringe pump (PHD ULTRA; Harvard Apparatus) was lowered into the guide cannula previously implanted over the MFB (depth -4.8 mm from brain surface). 750 nl of 6-OHDA solution (2.5 μg/μl for locomotion measurement; 1.25 μg/μl for reversal-learning task) was bilaterally infused into the MFB at a rate of 150 nl/min. Sham-operated control mice underwent similar procedures and were injected with vehicle (saline with 0.02% sodium ascorbate) instead of 6-OHDA. After infusion, the body mass of each animal was carefully monitored and a nutritionally fortified water gel (DietGel Recovery; ClearH_2O) was provided in conjunction with a shallow water dish and moist mouse chow to aid recovery. Recordings and locomotion measurements were performed 7-10 days after 6-OHDA infusion. Reversal-learning task was performed 3 days after 6-OHDA infusion.

SHIELD-MAP tissue processing

PV^{Cre} mice injected with AAV-FLEX-mRuby2-T2A-Synaptophysin-eGFP were processed for SHIELD-MAP as previously described (Park *et al.*, 2018). In brief, mice were deeply anesthetized with isoflurane and were transcardially perfused with 10 ml of ice-cold PBS followed by 20 ml of freshly-made ice-cold SHIELD perfusion solution. The brains were carefully extracted and post-fixed in the same solution at 4°C for 48 hours. The brains were cut parasagittally into 3-mm blocks, containing the GPe, SNr, and PF and transferred to a new conical tube with 20 ml of ice-cold SHIELD Off solution and incubated at 4°C for 24 hours. Brain blocks were then incubated in SHIELD On solution at 37°C for 24 hours and washed in PBS containing 0.02% sodium azide (Sigma) overnight at room temperature (RT). Subsequently, the samples were cleared with SDS clearing buffer for 10 days at 45°C while shaking, then washed overnight at RT with PBS containing 1% (v/v) Triton-X 100 (Sigma) and then with PBS. The samples were then incubated in monomer solution at 4°C for 3 days and were gel-embedded under nitrogen gas purge at 33°C for 4 hours. The samples were rehydrated in PBS for several hours and transferred to deionized water for tissue expansion. A light-sheet microscope (SmartSPIM; Life Canvas Technologies) with a 10x, 0.6 NA objective (Olympus) was used to obtain images from expanded samples. Formulas for all solutions and a detailed protocol can be found at chunglabresources.com.

Histology

After designated time for viral expression in tracing experiments or immediately after behavioral experiments, mice were deeply anesthetized with isoflurane and were transcardially perfused with ice-cold 4% paraformaldehyde in PBS. Brains were carefully extracted and post-fixed in the same fixative at 4°C for at least 12 hours. Brains were sliced at 60 μm thickness with a vibratome (VT1000; Leica). Brain sections were mounted on glass slides (SuperFrost Plus;

Fisher Scientific) or collected and stored in cryoprotectant (30% ethylene glycol, 30% glycerol in PBS) at -20°C for immunohistochemistry. Mounted slides were coverslipped with DAPI Fluoromount-G (Southern Biotech) and imaged with a 10x objective on an Olympus VS120 virtual slide microscope.

Tyrosine hydroxylase immunoreactivity

Quantification of striatal tyrosine hydroxylase (TH) immunoreactivity was used to assess the degree of dopamine depletion. Immunohistochemistry was carried out in free-floating fixed brain sections containing the dorsal striatum. The sections were washed with PBS for 3 times (10 min each) and incubated at room temperature for 1 hour in blocking solution containing 10% normal horse serum (Abcam), 0.2% bovine serum albumin (Sigma), and 0.5% Triton-X 100 (Sigma) in PBS. The sections were then incubated at 4°C for 20 hours in carrier solution containing 1% normal horse serum, 0.2% bovine serum albumin, and 0.5% Triton-X 100 in PBS with anti-TH primary antibody (1:2000; Millipore AB152). The sections were washed in PBS for 3 times and were incubated in carrier solution containing Alexa-flour 647-conjugated donkey anti-rabbit secondary antibody (1:1000; Life Technologies A-31573) at room temperature for 2 hours. Finally, the section washed 2 times in PBS, mounted, coverslipped, and imaged as described above. Each slide always included sections from naïve control animals that were processed and imaged in parallel to use as a reference. We used the pixel-intensity measuring tool in Fiji (ImageJ) to analyze fluorescence intensity from a 500 x 500 μm area taken from both hemispheres of each section. The fluorescence intensity for each section was normalized to the intensity of the naïve control tissue from the same slide. For locomotion measurements, all data included in the analysis were from mice with <35% TH immunoreactivity. For reversal-learning task, all data included in analysis were from mice with <70% TH immunoreactivity.

Multiplex *in situ* hybridization

Mice that underwent surgeries for mapping of the input-output relationship were deeply anesthetized with isoflurane and transcardially perfused with ice-cold PBS. The brains were extracted, submerged in embedding medium (Tissue-Tek O.C.T.; Sakura), and frozen with 2-methylbutane (Sigma) chilled with dry ice in 70% ethanol. The frozen brain blocks were stored at -20°C for at least one day, then sliced with a cryostat microtome (Thermo-Fisher) to obtain 20-μm coronal sections. For each brain, 8 sections regularly sampled across the entire dorsal striatum were mounted on SuperFrost Plus slides (Fisher Scientific) and processed exactly as described in the RNAscope assay online protocol (ACD; Advanced Cell Diagnostics). We used probe against eGFP mRNA to label striatal neurons infected with RVΔG-eGFP(EnvA) that spread trans-synaptically from either $PV^{GPe\text{-}SNr}$ or $PV^{GPe\text{-}PF}$ starter cells. Probes against *Drd1a* and *Drd2* mRNAs were used to determine whether the labeled striatal neurons were dMSNs or iMSNs. All probes were purchased from ACD. Because the labeling of eGFP mRNA was the strongest, we assigned the Atto-647 secondary probe to the eGFP probe to prevent bleed-through of the fluorescent signal into neighboring channels during imaging. Images of the entire dorsal striatum were acquired through a 30x silicone-immersion objective on a confocal microscope (Fluoview FV1200; Olympus). All eGFP-labeled neurons were manually quantified and classified as either dMSN or iMSN.

Quantification of input-output relationship

All sections except the olfactory bulb and the cerebellum were collected and processed as described in the 'Histology' section. All eGFP-labeled neurons from all brain regions except the GPe (injection site of the rabies virus) were quantified and presented as a percentage of total eGFP-labeled neurons from each brain. Brain regions were assigned based on the Franklin and Paxinos

Mouse Brain Atlas. Regions with <1% of total eGFP-labeled neurons were not included in the summary plot.

***Ex vivo* electrophysiology**

Mice were anesthetized with isoflurane and transcardially perfused with ice-cold choline-based slicing solution, containing (in mM): 25 $NaHCO_3$, 1.25 NaH_2PO_4, 2.5 KCl, 7 $MgCl_2$, 25 glucose, 0.5 $CaCl_2$, 110 choline chloride, 11.6 sodium ascorbate, and 3.1 sodium pyruvate. Brains were carefully extracted and transferred to a chamber filled with the same solution on a vibratome (VT1200; Leica). Brains were sliced at 250 μm (coronally for recording of target neurons, parasagittally for $PV^{GPe\text{-}SNr}$ neurons, and horizontally for $PV^{GPe\text{-}PF}$ neurons) and incubated at 35°C for 15-20 min in recovery solution, containing (in mM): 118 NaCl, 2.6 $NaHCO_3$, 11 glucose, 15 HEPES, 2.5 KCl, 1.25 NaH_2PO_4, 2 sodium pyruvate, 0.4 sodium ascorbate, 2 $CaCl_2$, and 1 $MgCl_2$. Slices were maintained at room temperature for at least one hour until transferred to a recording chamber an Olympus BX51WI upright microscope. The chamber was continuously superfused with artificial cerebrospinal fluid (ACSF), containing (in mM): 125 NaCl, 25 $NaHCO_3$, 2.5 KCl, 1.25 NaH_2PO_4, 11 glucose, 1.3 $MgCl_2$, and 2.5 $CaCl_2$, maintained at 30 ± 2°C by a feedback temperature controller. Slicing solution, recovery solution, and ACSF were constantly bubbled with 95% O_2 and 5% CO_2. All compounds were purchased from Tocris or Sigma.

For all recordings, patch pipettes (3-5 MΩ) were pulled from borosilicate glass (G150TF-4; Warner Instruments) with a DMZ Universal Electrode Puller (Zeitz Instruments) and filled with appropriate intracellular solutions. Liquid junction potential (5-8 mV) was not corrected for any experiments. Neurons were visualized with differential interference contrast optics or epifluorescence (Olympus). Recordings were made with a MultiClamp700B amplifier and pClamp10 software (Molecular Devices). Data were low-pass filtered at 1 kHz and digitized at 10

kHz with a digitizer (Digidata 1440; Molecular Devices). Series resistance was monitored and cells that displayed > 20% change over the duration of recording were excluded.

For current-clamp recording, pipettes were filled with an intracellular solution containing (in mM): 125 K^+-gluconate, 4 NaCl, 10 HEPES, 0.5 EGTA, 20 KCl, 4 Mg^{2+}-ATP, 0.3 Na^+-GTP, and 10 Na_2-phosphocreatine (290-300 mOsm, pH 7.2). Autonomous firing activity was acquired in a cell-attached configuration for 1 min prior to break-in. To measure the firing capacity of identified $PV^{GPe\text{-}SNr}$ and $PV^{GPe\text{-}PF}$ neurons, baseline firing was maintained at 5Hz and currents of increasing intensity (20 pA increments, duration = 500 ms) were injected until neurons went into depolarization block. All current-clamp recordings were performed in the presence of 5 μM NBQX and 50 μM picrotoxin to block synaptic transmission. Detection of spikes and measurements of action potential (AP) characteristics were performed using a custom Python script with the following criteria. AP threshold was measured as a change in voltage from rest at which the slope = 20 mV/ms. Peak amplitude was measured as a change in voltage from AP threshold to the peak of AP, and afterhyperpolarization (AHP) as a change in voltage and time from threshold to minimum after the peak. Half-width was calculated as full-width at half max amplitude. All measurements were quantified while neurons were firing at 5Hz.

Passive membranes properties were calculated from voltage-clamp recordings with a custom Python script based on previously described method (Hernández *et al.*, 2015); membrane resistance (R_m) was calculated by $R_m = \Delta V_{test}/\Delta I$ where ΔV_{test} is a 10-mV step (50 ms), and ΔI is a difference between steady-state current and baseline during the last 10 ms of the voltage step. Membrane capacitance (C_m) was calculated by $C_m = Q_t * \Delta V_{test}$ where Q_t is the integral of the transient current elicited by ΔV_{test}, a 10-mV voltage step (50 ms).

To measure the ratio of excitatory and inhibitory inputs (E/I ratio), pipettes were filled with a Cs-based intracellular solution, containing (in mM): 115 Cs^{+}-methanesulphonate, 10 HEPES, 1 EGTA, 1.5 MgCl2, 4 Mg^{2+}-ATP, 0.3 Na^{+}-GTP, 10 Na_2-phosphocreatine, 2 QX 314-Cl, 10 BAPTA-tetracesium (295 mOsm, pH 7.35). Electrically-evoked excitatory postsynaptic and inhibitory postsynaptic currents (EPSCs and IPSCs, respectively) were recorded from identified $PV^{GPe\text{-}SNr}$ and $PV^{GPe\text{-}PF}$ neurons at -60 mV (for EPSCs) and 0 mV (for IPSCs). E/I ratio was calculated by dividing the amplitude of EPSC by the amplitude of IPSC. Spontaneous EPSC and IPSC were also recorded at -60 mV and 0 mV, respectively.

For the recording of Sr^{2+}-induced asynchronous optogenetically-evoked postsynaptic currents, pipettes were filled with high-chloride intracellular solution, containing (in mM): 122 CsCl, 8 NaCl, 10 glucose, 1 $CaCl_2$, 10 HEPES, 10 EGTA, 2 Mg^{2+}-ATP, 0.3 Na^{+}-GTP, 2 QX 314-Cl (280-290 mOsm, pH 7.2). Slices were incubated with Ca^{2+}-free ACSF containing 4 mM $SrCl_2$ for 30 min before recording. oChIEF-expressing axon terminals were stimulated with a 5-ms blue light pulse emitted from a collimated light-emitting diode (473 nm; Thorlabs) driven by a T-Cube LED Driver (Thorlabs) under the control of Digidata 1440A Data Acquisition System and pClamp10 software (Molecular Devices). Light was delivered through the reflected light fluorescence illuminator port and the 40X objective at maximum intensity (13.45 mW). Recordings of optogenetically-evoked IPSCs were obtained from SNr or PF neurons located close to mCitrine-labeled axons in the presence of 5 μM NBQX. IPSC events were analyzed using a custom Python script based on previously described method (Tanimura *et al.*, 2019); the best fit curve of the largest evoked transient was subtracted from the original trace and the amplitude and frequency of IPSC events were measured between 20ms and 500ms after photostimulation. Target recordings in the SNr or PF neurons were performed similarly in a regular ACSF.

Behavioral assay: locomotion

Locomotion measurements in freely moving mice were performed in an open field arena (opaque white acrylic; w: 30 cm, L: 30 cm, H: 30 cm). To acclimate mice to the arena, we allowed them to freely explore the arena for 1 hour per day for 3 consecutive days. Baseline locomotor activity was obtained on the next day from 10-60 min after start during a 1-hour session. On subsequent days, the mice were tested based on their behavioral manipulation (see experimental timeline in Figure 4-5 and 7). The activity was recorded as a movie from overhead with a 15 Hz frame rate. The center point of each mouse in each frame was tracked off-line using Viewer II software (Biobserve) and was exported as raw data. Locomotor activity was then calculated using a custom Python script as speed in centimeter per second.

Behavioral assay: reversal-learning task

Mice were tested on a modified version of naturalistic foraging reversal discrimination task originally developed for rats (Birrell and Brown, 2000; McAlonan and Brown, 2003) and adapted for mice (Colacicco *et al.*, 2002; Garner *et al.*, 2006). Mice were food deprived to reduce body weight to 80-85% of the *ad libitum* feeding weight and habituate with a small animal food bowl (All Living Things Nibble bowls; PetSmart) used during the task for 7 days in their home cage prior to testing. During the same 7-day period, each mouse was handled for 1 min per day to minimize stress associated with handling during testing. One day before testing, mice were acclimated to a testing chamber (opaque white acrylic; w: 30 cm, L: 60 cm, H: 30 cm). Each mouse was placed in a waiting area separated from the rest of the testing chamber by a removable start gate. At the start of each trial, the gate was lifted and the mouse was allowed to explore two bowls placed at the opposite end of the chamber until a food reward was found and consumed. Both bowls did not contain digging media and only one bowl contains a food reward (a piece of Honey

Nut Cheerios ~50 mg).

The task consists of two consecutive phases that were performed over a 2-day period. First, in the association phase, mice were trained to associate a certain cue with a rewarding outcome, and a different cue without reward until they can discriminate reliably. In the subsequent reversal-learning phase, the cue-outcome associations were reversed, and thus, the mice needed to switch their actions to obtain the reward. The cues were either olfactory (odor) or somatosensory (texture of the digging medium which hides the bait). When the olfactory cues were used, one bowl contained coconut-scented soft bedding (National Geographic) and the other contained lavender-scented soft bedding (National Geographic). When the somatosensory cues were used, one bowl contained aquarium sand (National Geographic) and the other contained aquarium gravel. Only one type of cue was used with each mouse for the entire period of the task. All cues are presented in identical small animal food bowls (All Living Things Nibble bowls; PetSmart) that are identical in color and size. Digging media are mixed with the Honey Nut Cheerio powder (0.1% by volume).

On the first testing day (association), during each trial, the mouse was kept in the waiting area and two bowls were present at the opposite end of the chamber separated from the mouse by the start gate. At the start of each trial, the gate was lifted and the mouse is allowed to explore two bowls until digging in one bowl to signify a choice. The food reward was paired with a certain cue throughout the and was hidden in the digging medium. The baited bowl was pseudorandomly presented on either side of the testing cage. The mouse was required to choose the correct cue that would result in getting a food reward. The association phase was complete when a criterion of eight correct trials in a block of ten trials is met. On the second day (reversal learning), the mouse was presented with the same set of cues in the association phase but the cue-reward pairing is reversed. Similar criterion was required to complete the reversal-learning phase.

The number of correct and incorrect choice during each phase was scored manually and the performance of each mouse was reflected by the number of trials needed per phase to meet the criterion. Similar to previous findings, we observed an increase in the number of trials to criterion if odor is the relevant cue (Heisler *et al.*, 2015). Therefore, performance data for each mouse was normalized to an average number of trials to criterion from all naïve control mice (control mice that did not receive photostimulation or CNO) that were presented with a similar type of cue (odor or somatosensory) during the task.

Optogenetic stimulation

A 473 nm blue laser diode (OEM Laser Systems) was connected to the ferrule of the optic fiber previously implanted on mice though a plastic sleeve. Laser power was measured before each experiment and adjusted to ~8 mW. For all experiments with photostimulation, a train 500ms-pulses repeated every 1.5 s was used and was generated with a TTL pulse generator (OPT_G4; Doric Lenses). For locomotion assay, light pulses were delivered for from 30-40 min during a 1-hour session. For the reversal-learning task, light pulses were delivered for the entire duration of each trial during the reversal-learning phase.

Chemogenetic inhibition

Clozapine-N-oxide (CNO, Enzo) was dissolved in water to obtain a stock concentration of 5 mg/ml and stored in small aliquots at -20°C. The working solution was freshly prepared before each use by dilution the stock with 0.9% saline to obtain a concentration of 0.5 mg/ml. Mice were injected with 0.01 ml/g body weight of the working solution to achieve a dose of 5 mg/kg. For locomotion assay, on the first test day, mice were injected with saline 1 hour before testing. On the second day, mice were injected with the working solution 1 hour before testing. For the

reversal-learning task, mice were injected with the working solution 1 hour before the first trial of the reversal-learning phase.

Statistics

Statistical analyses were performed using Prism 8 (Graphpad Software). All statistical data can be found in figure legends with corresponding sample sizes. The sample sizes were chosen based on common practice in mouse behavioral experiments. All data were tested for normality with Shapiro-Wilk test. Then the appropriate parametric or non-parametric tests were applied. Correction for multiple comparisons was performed using the Bonferroni method. All statistical tests were two-tailed. Statistical significance levels were set at $*p < 0.05$, $**p < 0.01$, $***p < 0.001$. All data are presented as mean ± SEM.

Chapter 3, in full, is currently being prepared for submission for publication of the material. Lilascharoen, Varoth; Wang, Eric; Do, Nam; Pate, Stefan; Tran, Amanda; Wang, Xiao-Yun; Park, Young-Gyun; Lim, Byungkook. The dissertation author was the primary investigator and author of this material.

REFERENCES

Abdi, A., Mallet, N., Mohamed, F. Y., Sharott, A., Dodson, P. D., Nakamura, K. C., Suri, S., Avery, S. V., Larvin, J. T., Garas, F. N., Garas, S. N., Vinciati, F., Morin, S., Bezard, E., Baufreton, J. and Magill, P. J. (2015) 'Prototypic and arkypallidal neurons in the dopamine-intact external globus pallidus', *J Neurosci,* 35(17), pp. 6667-88.

Albin, R. L., Young, A. B. and Penney, J. B. (1989) 'The functional anatomy of basal ganglia disorders', *Trends Neurosci,* 12(10), pp. 366-75.

Albin, R. L., Young, A. B. and Penney, J. B. (1995) 'The functional anatomy of disorders of the basal ganglia', *Trends Neurosci,* 18(2), pp. 63-4.

Alexander, G. E., Crutcher, M. D. and DeLong, M. R. (1990) 'Basal ganglia-thalamocortical circuits: parallel substrates for motor, oculomotor, "prefrontal" and "limbic" functions', *Prog Brain Res,* 85, pp. 119-46.

Beier, K. T., Kim, C. K., Hoerbelt, P., Hung, L. W., Heifets, B. D., DeLoach, K. E., Mosca, T. J., Neuner, S., Deisseroth, K., Luo, L. and Malenka, R. C. (2017) 'Rabies screen reveals GPe control of cocaine-triggered plasticity', *Nature,* 549(7672), pp. 345-350.

Birrell, J. M. and Brown, V. J. (2000) 'Medial frontal cortex mediates perceptual attentional set shifting in the rat', *J Neurosci,* 20(11), pp. 4320-4.

Bissonette, G. B., Martins, G. J., Franz, T. M., Harper, E. S., Schoenbaum, G. and Powell, E. M. (2008) 'Double dissociation of the effects of medial and orbital prefrontal cortical lesions on attentional and affective shifts in mice', *J Neurosci,* 28(44), pp. 11124-30.

Bissonette, G. B., Schoenbaum, G., Roesch, M. R. and Powell, E. M. (2015) 'Interneurons are necessary for coordinated activity during reversal learning in orbitofrontal cortex', *Biol Psychiatry,* 77(5), pp. 454-64.

Bolam, J. P., Hanley, J. J., Booth, P. A. and Bevan, M. D. (2000) 'Synaptic organisation of the basal ganglia', *J Anat,* 196 (Pt 4), pp. 527-42.

Bradfield, L. A., Bertran-Gonzalez, J., Chieng, B. and Balleine, B. W. (2013) 'The thalamostriatal pathway and cholinergic control of goal-directed action: interlacing new with existing learning in the striatum', *Neuron,* 79(1), pp. 153-66.

Breese, G. R. and Traylor, T. D. (1971) 'Depletion of brain noradrenaline and dopamine by 6-hydroxydopamine', *Br J Pharmacol,* 42(1), pp. 88-99.

Brown, H. D., Baker, P. M. and Ragozzino, M. E. (2010) 'The parafascicular thalamic nucleus concomitantly influences behavioral flexibility and dorsomedial striatal acetylcholine output in rats', *J Neurosci,* 30(43), pp. 14390-8.

Brown, P., Oliviero, A., Mazzone, P., Insola, A., Tonali, P. and Di Lazzaro, V. (2001) 'Dopamine dependency of oscillations between subthalamic nucleus and pallidum in Parkinson's disease', *J Neurosci,* 21(3), pp. 1033-8.

Calabresi, P., Picconi, B., Tozzi, A., Ghiglieri, V. and Di Filippo, M. (2014) 'Direct and indirect pathways of basal ganglia: a critical reappraisal', *Nat Neurosci,* 17(8), pp. 1022-30.

Cazorla, M., de Carvalho, F. D., Chohan, M. O., Shegda, M., Chuhma, N., Rayport, S., Ahmari, S. E., Moore, H. and Kellendonk, C. (2014) 'Dopamine D2 receptors regulate the anatomical and functional balance of basal ganglia circuitry', *Neuron,* 81(1), pp. 153-64.

Cetin, A. and Callaway, E. M. (2014) 'Optical control of retrogradely infected neurons using drug-regulated "TLoop" lentiviral vectors', *J Neurophysiol,* 111(10), pp. 2150-9.

Colacicco, G., Welzl, H., Lipp, H. P. and Würbel, H. (2002) 'Attentional set-shifting in mice: modification of a rat paradigm, and evidence for strain-dependent variation', *Behav Brain Res,* 132(1), pp. 95-102.

Cools, R., Barker, R. A., Sahakian, B. J. and Robbins, T. W. (2001) 'Enhanced or impaired cognitive function in Parkinson's disease as a function of dopaminergic medication and task demands', *Cereb Cortex,* 11(12), pp. 1136-43.

Correia, S., Hubbard, E., Hassenstab, J., Yip, A., Vymazal, J., Herynek, V., Giedd, J., Murphy, D. L. and Greenberg, B. D. (2010) 'Basal ganglia MR relaxometry in obsessive-compulsive disorder: T2 depends upon age of symptom onset', *Brain Imaging Behav,* 4(1), pp. 35-45.

DeLong, M. R. (1990) 'Primate models of movement disorders of basal ganglia origin', *Trends Neurosci,* 13(7), pp. 281-5.

Ding, J. B., Guzman, J. N., Peterson, J. D., Goldberg, J. A. and Surmeier, D. J. (2010) 'Thalamic gating of corticostriatal signaling by cholinergic interneurons', *Neuron,* 67(2), pp. 294-307.

Dodson, P. D., Larvin, J. T., Duffell, J. M., Garas, F. N., Doig, N. M., Kessaris, N., Duguid, I. C., Bogacz, R., Butt, S. J. and Magill, P. J. (2015) 'Distinct developmental origins manifest in the specialized encoding of movement by adult neurons of the external globus pallidus', *Neuron,* 86(2), pp. 501-13.

Garner, J. P., Thogerson, C. M., Würbel, H., Murray, J. D. and Mench, J. A. (2006) 'Animal neuropsychology: validation of the Intra-Dimensional Extra-Dimensional set shifting task for mice', *Behav Brain Res,* 173(1), pp. 53-61.

Grabli, D., McCairn, K., Hirsch, E. C., Agid, Y., Féger, J., François, C. and Tremblay, L. (2004) 'Behavioural disorders induced by external globus pallidus dysfunction in primates: I. Behavioural study', *Brain,* 127(Pt 9), pp. 2039-54.

Grospe, G. M., Baker, P. M. and Ragozzino, M. E. (2018) 'Cognitive Flexibility Deficits Following 6-OHDA Lesions of the Rat Dorsomedial Striatum', *Neuroscience,* 374, pp. 80-90.

Haber, S. N. and Calzavara, R. (2009) 'The cortico-basal ganglia integrative network: the role of the thalamus', *Brain Res Bull,* 78(2-3), pp. 69-74.

Hammond, C., Bergman, H. and Brown, P. (2007) 'Pathological synchronization in Parkinson's disease: networks, models and treatments', *Trends Neurosci,* 30(7), pp. 357-64.

Hegeman, D. J., Hong, E. S., Hernández, V. M. and Chan, C. S. (2016) 'The external globus pallidus: progress and perspectives', *Eur J Neurosci,* 43(10), pp. 1239-65.

Heisler, J. M., Morales, J., Donegan, J. J., Jett, J. D., Redus, L. and O'Connor, J. C. (2015) 'The attentional set shifting task: a measure of cognitive flexibility in mice', *J Vis Exp,* (96).

Hernández, V. M., Hegeman, D. J., Cui, Q., Kelver, D. A., Fiske, M. P., Glajch, K. E., Pitt, J. E., Huang, T. Y., Justice, N. J. and Chan, C. S. (2015) 'Parvalbumin+ Neurons and Npas1+ Neurons Are Distinct Neuron Classes in the Mouse External Globus Pallidus', *J Neurosci,* 35(34), pp. 11830-47.

Hikosaka, O., Nakamura, K. and Nakahara, H. (2006) 'Basal ganglia orient eyes to reward', *J Neurophysiol,* 95(2), pp. 567-84.

Hintiryan, H., Foster, N. N., Bowman, I., Bay, M., Song, M. Y., Gou, L., Yamashita, S., Bienkowski, M. S., Zingg, B., Zhu, M., Yang, X. W., Shih, J. C., Toga, A. W. and Dong, H. W. (2016) 'The mouse cortico-striatal projectome', *Nat Neurosci,* 19(8), pp. 1100-14.

Johnson, M. D., Zhang, J., Ghosh, D., McIntyre, C. C. and Vitek, J. L. (2012) 'Neural targets for relieving parkinsonian rigidity and bradykinesia with pallidal deep brain stimulation', *J Neurophysiol,* 108(2), pp. 567-77.

Kato, S., Fukabori, R., Nishizawa, K., Okada, K., Yoshioka, N., Sugawara, M., Maejima, Y., Shimomura, K., Okamoto, M., Eifuku, S. and Kobayashi, K. (2018) 'Action Selection and Flexible Switching Controlled by the Intralaminar Thalamic Neurons', *Cell Rep,* 22(9), pp. 2370-2382.

Kato, S. and Kobayashi, K. (2014) 'Improved transduction efficiency of a lentiviral vector for neuron-specific retrograde gene transfer by optimizing the junction of fusion envelope glycoprotein', *J Neurosci Methods,* 227, pp. 151-8.

Kato, S., Kuramochi, M., Kobayashi, K., Fukabori, R., Okada, K., Uchigashima, M., Watanabe, M. and Tsutsui, Y. (2011) 'Selective neural pathway targeting reveals key roles of thalamostriatal projection in the control of visual discrimination', *J Neurosci,* 31(47), pp. 17169-79.

Kita, H. (2007) 'Globus pallidus external segment', *Prog Brain Res,* 160, pp. 111-33.

Kita, H. and Kitai, S. T. (1994) 'The morphology of globus pallidus projection neurons in the rat: an intracellular staining study', *Brain Res,* 636(2), pp. 308-19.

Knowland, D., Lilascharoen, V., Pacia, C. P., Shin, S., Wang, E. H. and Lim, B. K. (2017) 'Distinct Ventral Pallidal Neural Populations Mediate Separate Symptoms of Depression', *Cell,* 170(2), pp. 284-297 e18.

Kreitzer, A. C. and Berke, J. D. (2011) 'Investigating striatal function through cell-type-specific manipulations', *Neuroscience,* 198, pp. 19-26.

Lim, B. K., Huang, K. W., Grueter, B. A., Rothwell, P. E. and Malenka, R. C. (2012) 'Anhedonia requires MC4R-mediated synaptic adaptations in nucleus accumbens', *Nature,* 487(7406), pp. 183-9.

Lin, J. Y., Lin, M. Z., Steinbach, P. and Tsien, R. Y. (2009) 'Characterization of engineered channelrhodopsin variants with improved properties and kinetics', *Biophys J,* 96(5), pp. 1803-14.

Mahn, M., Prigge, M., Ron, S., Levy, R. and Yizhar, O. (2016) 'Biophysical constraints of optogenetic inhibition at presynaptic terminals', *Nat Neurosci,* 19(4), pp. 554-6.

Mallet, N., Micklem, B. R., Henny, P., Brown, M. T., Williams, C., Bolam, J. P., Nakamura, K. C. and Magill, P. J. (2012) 'Dichotomous organization of the external globus pallidus', *Neuron,* 74(6), pp. 1075-86.

Mallet, N., Pogosyan, A., Márton, L. F., Bolam, J. P., Brown, P. and Magill, P. J. (2008a) 'Parkinsonian beta oscillations in the external globus pallidus and their relationship with subthalamic nucleus activity', *J Neurosci,* 28(52), pp. 14245-58.

Mallet, N., Pogosyan, A., Sharott, A., Csicsvari, J., Bolam, J. P., Brown, P. and Magill, P. J. (2008b) 'Disrupted dopamine transmission and the emergence of exaggerated beta oscillations in subthalamic nucleus and cerebral cortex', *J Neurosci,* 28(18), pp. 4795-806.

Mastro, K. J., Bouchard, R. S., Holt, H. A. and Gittis, A. H. (2014) 'Transgenic mouse lines subdivide external segment of the globus pallidus (GPe) neurons and reveal distinct GPe output pathways', *J Neurosci,* 34(6), pp. 2087-99.

McAlonan, K. and Brown, V. J. (2003) 'Orbital prefrontal cortex mediates reversal learning and not attentional set shifting in the rat', *Behav Brain Res,* 146(1-2), pp. 97-103.

Oliet, S. H., Malenka, R. C. and Nicoll, R. A. (1996) 'Bidirectional control of quantal size by synaptic activity in the hippocampus', *Science,* 271(5253), pp. 1294-7.

Osakada, F. and Callaway, E. M. (2013) 'Design and generation of recombinant rabies virus vectors', *Nat Protoc,* 8(8), pp. 1583-601.

Park, Y. G., Sohn, C. H., Chen, R., McCue, M., Yun, D. H., Drummond, G. T., Ku, T., Evans, N. B., Oak, H. C., Trieu, W., Choi, H., Jin, X., Lilascharoen, V., Wang, J., Truttmann, M. C., Qi, H. W., Ploegh, H. L., Golub, T. R., Chen, S. C., Frosch, M. P., Kulik, H. J., Lim, B. K. and Chung, K. (2018) 'Protection of tissue physicochemical properties using polyfunctional crosslinkers', *Nat Biotechnol*.

Parker, P. R., Lalive, A. L. and Kreitzer, A. C. (2016) 'Pathway-Specific Remodeling of Thalamostriatal Synapses in Parkinsonian Mice', *Neuron,* 89(4), pp. 734-40.

Peterson, D. A., Elliott, C., Song, D. D., Makeig, S., Sejnowski, T. J. and Poizner, H. (2009) 'Probabilistic reversal learning is impaired in Parkinson's disease', *Neuroscience,* 163(4), pp. 1092-101.

Saunders, A., Huang, K. W. and Sabatini, B. L. (2016) 'Globus Pallidus Externus Neurons Expressing parvalbumin Interconnect the Subthalamic Nucleus and Striatal Interneurons', *PLoS One,* 11(2), pp. e0149798.

Saunders, A., Oldenburg, I. A., Berezovskii, V. K., Johnson, C. A., Kingery, N. D., Elliott, H. L., Xie, T., Gerfen, C. R. and Sabatini, B. L. (2015) 'A direct GABAergic output from the basal ganglia to frontal cortex', *Nature,* 521(7550), pp. 85-9.

Smith, Y., Bevan, M. D., Shink, E. and Bolam, J. P. (1998) 'Microcircuitry of the direct and indirect pathways of the basal ganglia', *Neuroscience,* 86(2), pp. 353-87.

Smith, Y., Galvan, A., Ellender, T. J., Doig, N., Villalba, R. M., Huerta-Ocampo, I., Wichmann, T. and Bolam, J. P. (2014) 'The thalamostriatal system in normal and diseased states', *Front Syst Neurosci,* 8, pp. 5.

Smith, Y., Surmeier, D. J., Redgrave, P. and Kimura, M. (2011) 'Thalamic contributions to Basal Ganglia-related behavioral switching and reinforcement', *J Neurosci,* 31(45), pp. 16102-6.

Tanimura, A., Du, Y., Kondapalli, J., Wokosin, D. L. and Surmeier, D. J. (2019) 'Cholinergic Interneurons Amplify Thalamostriatal Excitation of Striatal Indirect Pathway Neurons in Parkinson's Disease Models', *Neuron,* 101(3), pp. 444-458.e6.

Vitek, J. L., Hashimoto, T., Peoples, J., DeLong, M. R. and Bakay, R. A. (2004) 'Acute stimulation in the external segment of the globus pallidus improves parkinsonian motor signs', *Mov Disord,* 19(8), pp. 907-15.

Vitek, J. L., Zhang, J., Hashimoto, T., Russo, G. S. and Baker, K. B. (2012) 'External pallidal stimulation improves parkinsonian motor signs and modulates neuronal activity throughout the basal ganglia thalamic network', *Exp Neurol,* 233(1), pp. 581-6.

Wallace, M. L., Saunders, A., Huang, K. W., Philson, A. C., Goldman, M., Macosko, E. Z., McCarroll, S. A. and Sabatini, B. L. (2017) 'Genetically Distinct Parallel Pathways in the Entopeduncular Nucleus for Limbic and Sensorimotor Output of the Basal Ganglia', *Neuron,* 94(1), pp. 138-152.e5.